Article

Geochronology, Geochemistry, and Lu-Hf Isotopic Compositions of Monzogranite Intrusion from the Chang'anpu Mo Deposit, NE China: Implications for Tectonic Setting and Mineralization

Jian Zhang [1,2], Yanchen Yang [1,*], Shijiong Han [1] and Wukeyila Wutiepu [3]

[1] College of Earth Sciences, Jilin University, Changchun 130061, China; zj16@mails.jlu.edu.cn (J.Z.); hanshijiong@jlu.edu.cn (S.H.)

[2] Jilin Nonferrous Metal Geological Exploration Bureau, Team 607, Jilin 132000, China

[3] Xinjiang Research Centre for Mineral Resources, Xinjiang Institute of Ecology and Geography, Chinese Academy of Sciences, Urumqi 830011, China; wkylw@ms.xjb.ac.cn

* Correspondence: yyc@jlu.edu.cn; Tel.: +86-431-88502128

Abstract: The Chang'anpu Molybdenum deposit occurs in the monzogranite intrusions in the Lesser Khingan Mountains-Zhangguangcai Mountains metallogenic belt. Previous work focused on the study of deposits, including geological characteristics, mineralization time, S-Pb isotope, etc. However, systematic petrogeochemical study of monzogranite intrusion and comparative analysis with other porphyry deposits in the region are lacking. Three monzogranite dating samples yield LA-ICP-MS zircon weighted mean $^{206}Pb/^{238}U$ ages of 174.7 ± 1.3 Ma, 174.9 ± 1.4 Ma, and 174.3 ± 1.8 Ma, respectively, indicating that the magmatism occurred in the middle Jurassic of Mesozoic. The 14 monzogranite samples show alkali rich and relatively high silica content (up to 84.39%) with the differentiation index (DI) ranges from 86 to 96, showing that monzogranite have been subjected to fractional crystallization during its evolution; the depletion of Ba, Sr, P, Nb, Ti, and Eu also indicates that the rock has undergone crystallization fractionation, the monzogranite belong to the highly fractionated I-type. Positive $\varepsilon_{Hf}(t)$ values (6.72–8.85) and young T_{DM2} (551–673 Ma) of the monzogranite indicate that the formation of Chang'anpu monzogranite intrusion is related to the partial melting of juvenile lower crust, originated from the Mesoproterozoic depleted mantle. The magmatism and related Mo mineralization in the Chang'anpu deposit occurred in an active continental margin setting associated with westward subduction of the Paleo-Pacific plate beneath the Eurasian plate.

Keywords: monzogranite intrusion; zircon U-Pb and Lu-Hf isotopes; geochemistry; Chang'anpu Mo deposit; subduction of the Pacific plate

1. Introduction

Porphyry deposits have become the main source of copper and molybdenum resources in the world, and the main target of exploration due to their large reserves and wide distribution. Globally, economically important porphyry molybdenum deposits are mainly distributed in the Alpine fold belt, such as the Western Cordillera in North America, British Columbia in Canada, Southeast Alaska, and the Western United States. The three largest porphyry molybdenum deposits in the world, Climax, Urad-Hendeson, and Mt.Emmons, all occur in the Colorado molybdenum belt. Secondly, the Circum-Pacific metallogenic belt and Central Asian Orogenic Belt (CAOB) [1–6]. In China, porphyry molybdenum deposits are mainly distributed in East Qinling, Lesser Khingan Mountains-Zhangguangcai Mountains and Yanliao molybdenum belts. The molybdenum deposits in China are mainly the products of the late Indosinian to Yanshanian magmatism, which is different from the late Cretaceo-Oligocene molybdenum deposits in foreign countries [7–9]. The study of

geochronology and petrogeochemistry of intrusions which the porphyry deposits occurred in is not only helpful to understand the process of diagenesis and mineralization [10–15], but can also reflect the tectonic evolution process controlling the formation of intrusions and ore deposits [16–20].

Most porphyry deposits in both oceanic (e.g., Philippines, Indonesia) and continental (Andes) magmatic arcs, as well as accretionary belts of different age, are related one way or another to adakitic (high Sr/Y) magmatic rocks. These mainly include: Aginsky, Asachinsky, Ametistovy epithermal gold deposits in Cenozoic Kamchatka arc, Russian Far East; Santo Tomas II, Didipio porphyry-type copper-gold deposits in the Philippines; Kelian epithermal gold deposit in Indonesia; Escondida, Chuquicamata copper porphyry cluster in Andean magmatic arc; Pebble porphyry Cu–Au–Mo deposit in Southwestern Alaska, belong to the Circum-Pacific magmatic arcs; Erdenet and Oyu Tolgoi Cu–Au porphyry systems in Mongolia; and Bystrinsky Cu–Fe–Mo–Au deposit in the Trans-Baikal region, Central Asian Orogenic Belt [21]. Several porphyry molybdenum deposits, including Dongfengbeishan, Daheishan, Xingshan, Dashihe, Fu'anpu, Jidetun, Houdaomu, Liushengdian, Huojihe, Culing, and Luming etc., have been exploited in the Lesser Khingan Mountains-Zhangguangcai Mountains in NE China in recent years, making it an important Mo province in China [22–33] (Figure 1, Table 1). The age of the ore-forming rocks is mainly concentrated in the early-middle Jurassic due to the extensive development of Yanshanian fault structures and granitoid intrusions in Eastern China, such as Daheishan (granodiorite porphyry, 166.6 ± 4 Ma), Fu'anpu (porphyritic monzogranite, 166.9 ± 6.7 Ma), Jidetun (granodiorite, 180.2 ± 0.8), Xingshan (granodiorite porphyry, 171.7 ± 2.2 Ma), Huojihe (granodiorite, 181.0 ± 1.9 Ma), Luming (monzogranite porphyry, 183.2 ± 1.9 Ma), and Cuiling (quratz monzonite, 178.0 ± 0.7 Ma) (Figure 1, Table 1). The Cretaceous deposits are relatively few, represented by Xiaodonggou (138 ± 3 Ma). Through study of the geochemical characteristics of porphyry, metallogenic porphyry is mainly granodiorite, quartz monzonite, and quartz diorite, with a small amount of granite [34,35]. On the whole, the ore-forming rocks are mainly medium-acid calc-alkaline rocks, while the basic rocks and granites with high acidity are rarely reported. In terms of tectonic environment, the ore-forming porphyry bodies in a continental-margin-arc environment are mainly calc-alkaline series, while in an island-arc and orogenic belt they are characterized by high potassium, which can be divided into high-K calc-alkaline series and shoshonite series; the lithology is mainly granodiorite and monzogranite [24–28].

Table 1. Geochronology and tectonic setting of metallogenic porphyry in Early–Middle Jurassic nonferrous metal deposits in NE China.

No.	Typical Deposits	Mineral Type	Metallogenic Rock	Ages (Ma)	Tectonic Setting	References
1	Dongfengbeishan	Mo	Porphyritic monzogranite	195.6 ± 1.9	Extensional tectonic setting caused by subduction of the Pacific plate	[22]
2	Daheishan	Mo	Granodiorite porphyry	166.6 ± 4	Extensional tectonic setting caused by subduction of the Pacific plate	[23]
3	Xingshan	Mo	Granodiorite porphyry	171.7 ± 2.2	Active continental margin; related to subduction of the Pacific plate	[24]
4	Dashihe	Mo	Porphyritic granodiorite	186.7 ± 5	Extensional tectonic setting caused by subduction of the Pacific plate	[25]
5	Fu'anpu	Mo	Porphyritic monzogranite	166.9 ± 6.7	Extensional tectonic setting caused by subduction of the Pacific plate	[26]

Table 1. *Cont.*

No.	Typical Deposits	Mineral Type	Metallogenic Rock	Ages (Ma)	Tectonic Setting	References
6	Jidetun	Mo	Granodiorite	180.2 ± 0.8	Active continental margin; related to subduction of the Pacific plate	[27]
7	Chang'anpu	Mo	Monzogranite	174.3–174.9	Extensional tectonic setting caused by subduction of the Pacific plate	This study
8	Houdaomu	Mo	Yanshanian granite	167.5 ± 1.2	Extensional tectonic setting caused by subduction of the Pacific plate	[28]
9	Liushengdian	Mo	Monzogranite porphyry	169.4 ± 1.0	Volcanic arc setting; related to subduction of the Pacific plate	[29]
10	Luming	Mo	Monzogranite porphyry	183.2 ± 1.9	Volcanic arc setting; related to subduction of the Pacific plate	[30]
11	Huojihe	Mo	Granodiorite	181.0 ± 1.9	Volcanic arc setting; related to subduction of the Pacific plate	[31]
12	Cuiling	Mo	Quratz monzonite	178.0 ± 0.7	Volcanic arc setting; related to subduction of the Pacific plate	[32]

The Chang'anpu deposit is a newly discovered porphyry molybdenum deposit in Lesser Khingan Mountains-Zhangguangcai Mountains. Previous work focused on the study of this and similar deposits in the region, including geological characteristics, mineralization time, S-Pb isotope, etc., [28,36–40]; however, systematic petrogeochemical study of monzogranite intrusion and comparative analysis with other porphyry deposits in the region are lacking. In this study, we conducted detailed research of the monzogranite, the host rock of the Chang'anpu deposit, including U-Pb dating, geochemical analyses, and Hf isotopic compositional analyses, to systematically elucidate the geological age, petrogenetic type, magma source, and evolution of Chang'anpu monzogranite, as well as tectonic setting during the formation of regional large-scale metallogenic porphyry.
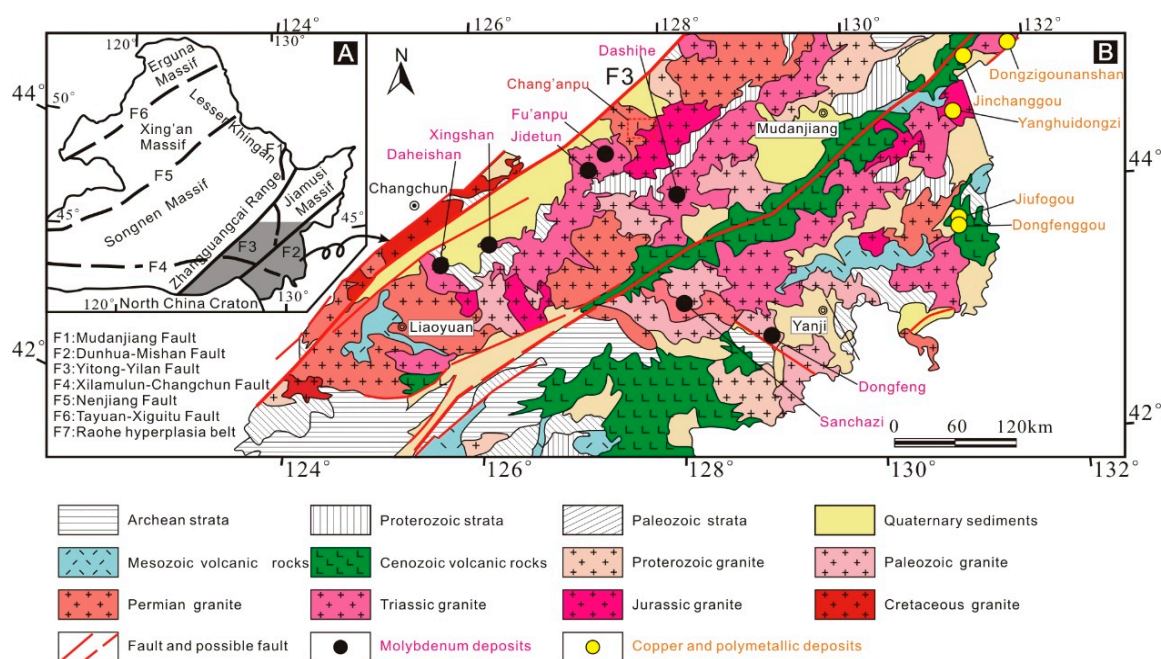

Figure 1. Simplified tectonic map (**A**), and geological map (**B**), of the Chang'anpu Mo deposit and adjacent areas (Modified after Han et al., 2013) [40].

2. Regional Geological Setting

The Central Asian Orogenic Belt (CAOB) is the largest accumulation of accreted terranes (island arcs, back-arc basins, oceanic plateaus and islands, micro-continents, etc.) on our planet, located between the East European and Siberian Cratons, and the North China-Tarim Craton. It was formed by the merging of different Paleozoic terranes under the progressive subduction of the Paleo-Asian Ocean plate [41–45]. Characteristics of the CAOB include the presence of juvenile crust and granites with relatively young Nd model ages [42,44,46–49]. The CAOB is richly endowed with Cu–Au–Mo porphyry and epithermal Au deposits of various size from the Paleozoic to Mesozoic age, many of which are associated with adakite magmatism [21,50–52]. The Porphyry deposits in CAOB are widely distributed, starting from Russia's Ural Mountains in the west, through Central Asia, China's Xinjiang and Inner Mongolia, to NE China in the east, spanning thousands of kilometers, and almost running through the whole Eurasia continent [32,53,54]. Most of these deposits in the CAOB were formed in subduction-accretion complex after the late Neoproterozoic. NE China, located at the eastern end of CAOB, was mainly formed during the Neoproterozoic to Late Paleozoic age. Its formation is related to the subduction of Paleo-Asian plate, the collision between the Siberian craton and North China Craton (NCC), and the amalgamation of microcontinental terranes, or massifs, such as Erguna, Hingan, Songliao, and Jimusi-Khanka (from west to east) [55–60] (Figure 1A). NE China has been modified and overprinted by the Paleo-Asian oceanic and the circum-Pacific tectonic system [61]; multiphasic tectonism had produced favorable space for the formation of porphyry intrusions and the clustering of porphyry deposits.

The Lesser Khingan Mountains-Zhangguangcai Mountains metallogenic belt belongs to the Songnen Massif, the whole metallogenic belt extend from Heilongjiang in the north, to the Jilin in the south in an arc shape of NNW-NS, with a total length of nearly 700 km and a maximum width of up to 100 km (Figure 1A).

The area has been subjected to intense sedimentation, folding and metamorphism at the Precambrian-Phanerozoic transition, followed by large-scale Paleozoic gabbro-granodiorite- granite magmatism, with predominant high-K calc-alkaline and shoshonitic chemistry [62]. During Mesozoic, it was involved in the development of multiple subduction zones and active continental margins related to the closure of the Mongol-Okhotsk Ocean, and the subduction of the Paleo-Pacific Ocean, and was marked by a calc-alkaline to shoshonitic volcanic series and associated granitoids [47,63–66].

The mining area has relatively simple lithology and undeveloped strata, all of which are Mesozoic granite intrusions; from west to east there are plagiogranite, monzogranite, and alkali-feldspar granite, and the Chang'anpu deposit is wholly hosted in monzogranite (Figure 2A). The orebody is stratified in space, with an E-W direction (Figure 2A,B). The ore is mainly disseminated. Metallic minerals are molybdenite, pyrite and a small amount of chalcopyrite, pyrrhotite, galena, and sphalerite. Faults that develop in this region are mainly compressional faults; the tectonic framework in this area is composed of the Xinan-Ermu fault in a NW direction and the Huoshidingzi- Chang'anpu fault in a NE direction. The Chang'anpu deposit is at the intersection of the two; fracture zone, argillic alteration and structural breccia are common in the deposit. An EW compressional fault, F1, has developed in the deposit, which is about 2 km long and 100 m to 200 m wide. It consists of a series of parallel fault zones, including fracture zone, gouge, scratch, tectonic breccia, and later, intrusive quartz vein. The F1 fault is a secondary structure of the NW-trending Xin'an-Ermu fault, and is the main rock-ore-controlling tectonic in this deposit, controlling the spatial morphology and distribution of ore bodies [36,39,40].
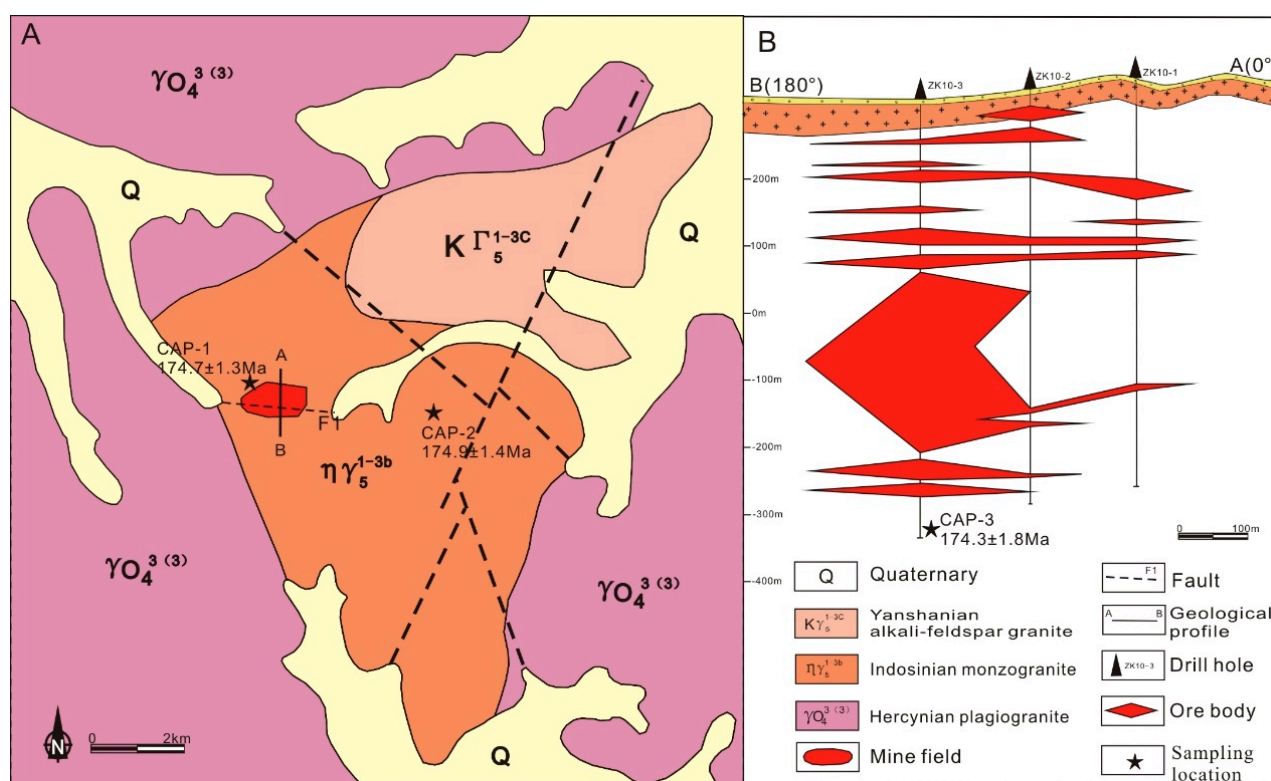
Figure 2. Regional geological and metallogenic map (**A**), and Exploration section map (**B**) in the Chang'anpu Mo deposit.

3. Petrological Characteristics

As the deposit is fully hosted in monzogranite intrusion, and the spatiotemporal distribution of monzogranite bodies has a large range, the samples of monzogranite in different locations and layers were selected to conduct geochronology and geochemical analyses. Three U–Pb dating samples and 14 geochemical samples were taken from positions near the surface (CAP-N1), deep through the ore body (CAP-N2, taken from 650 m of drill hole ZK10-3), and far away from the deposit (CAP-N3); the sample (CAP-N1) was used for Hf isotopic analysis. All samples were selected from unaltered or slightly altered monzogranite. Tthe sampling locations are shown in Figure 2A.

Monzogranite show a grayish-red, granular texture, and massive structure. The overall modal composition is: K-feldspars, xenomorphic granular textures, particle size 1.0–2.5 mm, content of about 30%–35% (in volume); Plagioclase grains, euhedral to subhedral, are partially altered to sericite, particle size 1.0–3.0 mm, content 25%–30%; quartz, anhedral granular texture, particle size 0.5–2.5 mm, content 25%–30%; Biotite is about 5%, partially altered to chlorite (Figure 3). The content of K-feldspars in the surrounding rock of the orebody was increased, and some parts of the rock were broken and re-cemented under the tectonic stress, which is of brecciform structure with quartz veins inserted into it.

Figure 3. Microphotographs and photographs of monzogranite in the Chang'anpu area. (**A**) monzogranite (hand specimen); (**B**) brecciated monzogranite (hand specimen); (**C**) photomicrograph of monzogranite adjacent to the ore body; (**D**) photomicrograph of monzogranite (cross-polarized light). Abbreviations: Qtz—quartz; Pl—plagioclase; Bt—biotite; Kfs—potash feldspar.

4. Analytical Methods

4.1. Major and Trace Element Determinations

The samples were analyzed in Hebei Institute of Geology and Mineral Resources, Langfang, China. Before testing, all the samples were pulverized into granules smaller than 200 mesh in agate mortars. The concentration of major oxides in the samples was analyzed by X-ray Fluorescence spectrometer (XRF) except FeO (wet chemical method). Inductively coupled plasma-mass spectrometry (ICP-MS) was selected to measure trace elements. Analysis precision of major and trace elements was better than 5% and 10%, respectively.

4.2. Zircon U–Pb Dating

After crushing the collected samples, conventional methods using flotation and magnetic separation were used. Samples were selected with binoculars, looking for a crystal shape and transparency, and being free of cracks of zircon grains. Using epoxy resin, and after grinding and polishing, reflected light and cathodoluminescence (CL) of the image was acquired. The transmitted and reflected light images of zircon were collected at the Comprehensive Identification Laboratory of Rock and Mineral Resources, College of Earth Sciences, Jilin University, while CL images and LA-ICP-MS U-Pb isotope analysis of zircon were collected at MLR Key Laboratory of Mineral Resources Evaluation in Northeast Asia, Jilin University, Changchun, China. Through the reflected light and CL images of zircon, the regions without cracks and inclusions, and with uniform absorption, were selected and analyzed using standard determination procedures on an Agilent 7500AICP-MS instrument. In the experiment, high purity He was used as the carrier gas of the denuded material; the standard reference substance NISTSRM610 of synthetic silicate glass, developed by the National Institute of Standards and Technology, was used to optimize the instrument.

Zircon standard samples were Plesovice (age 337 ± 0.37 Ma) [67]. NIST SRM 612 was used as the component standard, and ^{29}Si was used as the internal standard element. The laser spot diameter was 32 μm and data processing was performed using ICPMSDataCal [68,69]; general Pb calibration was carried out by Andersen (2002) [70]; age calculation harmony and plot drawing were completed by international standard program Isoplot (v3.0) [71]; the given isotope ratio and age error were all at the level of 1σ.

4.3. Lu–Hf Isotopic Analysis

Based on LA-ICP-MS zircon U-Pb dating, Hf isotopic compositions of zircon microregions were determined. In situ Lu-Hf isotopic analysis of zircons was performed, using laser-denuded multi-receiver plasma mass spectrometry (LA-MC-ICP-MS) at Northwestern University, Xi'an, China. MC-ICP-MS is all Neptune. For the 193 nm laser, helium gas was used as the carrier gas under given instrument conditions to improve signal sensitivity. In the single point ablation mode, the patches were fixed to 60 μm and 44 μm, respectively. For detailed instrument operating conditions and analysis methods, refer to Wu et al. (2006) [72]. In $\varepsilon_{Hf\,(t)}$ and model age calculation, the present $^{176}Lu/^{177}Hf$ and $^{176}Hf/^{177}Hf$ of the chondritic, and depleted mantle, are 0.0332, 0.282772 and 0.0384, 0.28325, respectively [73]. When calculating the two-stage model age (T_{DM2}), $^{176}Lu/^{177}Hf = 0.015$ was taken as the mean continental crust [74]. All zircons had low $^{176}Lu/^{177}Hf$ ratios, almost all of which were less than 0.002, indicating that zircons have low accumulation of radiological Hf after their formation. Offline processing of the analytical data, including sample and blank signal selection and isotope mass fractionation correction, was performed using software ICPMSDataCal [69].

5. Results

5.1. Major and Trace Element Geochemistry

The major and trace element contents of the monzogranite in Chang'anpu deposit are shown on Table 2, and plotted in Figure 4. According to the CIPW-NORM ratio of quartz to feldspar, the lithology is mainly monzogranite. The results of sample analysis showed high concentrations of SiO_2 (69.50–84.39 wt.%), Al_2O_3 (6.35–15.36 wt.%), and $Na_2O + K_2O$ (4.39–9.81 wt.%), and relatively low CaO (0.47–2.00 wt.%), MgO (0.13–0.67 wt.%), TiO_2 (0.06–0.37 wt.%), and P_2O_5 (0.01–0.15 wt.%) concentrations. The trace elements composition of mineralized monzonite is shown in Table 2; the REE content varies widely from 75.97 to 145.83 ppm, with a strong light rare earth element (LREE)/heavy rare earth element (HREE) fractionation ($(La/Yb)_N$ = 13.44–22.54). The chondrite-normalized REE patterns of monzogranite show a negative Eu anomaly (Eu/Eu* = 0.39–0.92) and LRRE enrichment over the HREE (Figure 4A). In the primitive-mantle-normalized trace elements diagram (Figure 4B), the monzogranite is enriched in Rb, Th, and K and relatively depleted in Nb, Ba, P, Sr, and Ti.
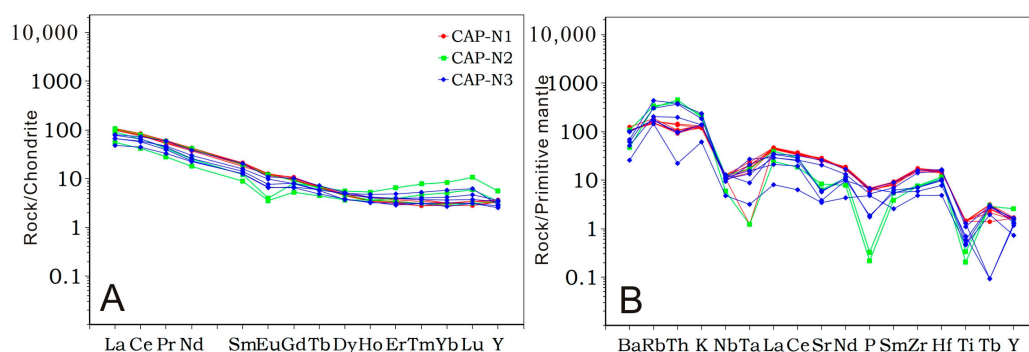

Figure 4. (**A**) Chondrite normalized REE pattern; (**B**) primitive mantle normalized trace element spider diagram of monzogranite in the Chang'anpu porphyry Mo deposit (Sun and McDonough, 1989) [75].

Table 2. Major oxides (wt.%) and trace elements (ppm) compositions for the Chang'anpu monzogranite.

Sample No.	N1-Q1	N1-Q2	N1-Q3	N1-Q4	N1-Q5	N1-Q6	N2-Q1	N2-Q2	N2-Q3	N3-Q1	N3-Q2	N3-Q3	N3-Q4	N3-Q5
SiO_2	69.81	70.22	70.11	70.36	70.03	69.50	73.48	75.42	70.19	69.76	72.16	84.39	74.78	71.33
Al_2O_3	15.24	15.20	15.36	14.93	15.30	15.02	13.93	13.08	15.21	15.00	14.28	6.35	11.96	13.12
TFe_2O_3	2.56	2.17	2.34	2.24	2.26	2.30	0.68	1.00	2.26	2.24	2.05	1.22	1.02	1.95
MgO	0.67	0.63	0.66	0.56	0.59	0.66	0.13	0.14	0.60	0.67	0.50	0.15	0.34	0.60
CaO	1.86	1.80	1.82	1.86	1.94	1.77	0.74	0.47	1.94	1.78	1.44	0.74	1.61	2.00
Na_2O	4.25	4.42	4.42	4.44	4.58	4.04	3.31	3.02	4.55	4.30	4.10	0.16	2.13	0.21
K_2O	3.58	3.77	3.69	3.73	3.70	4.10	6.50	5.88	3.63	4.13	4.22	4.23	5.57	7.19
MnO	0.02	0.02	0.02	0.02	0.02	0.03	0.02	0.01	0.02	0.02	0.02	0.02	0.02	0.03
TiO_2	0.37	0.34	0.35	0.33	0.34	0.37	0.06	0.07	0.34	0.35	0.29	0.19	0.19	0.16
P_2O_5	0.14	0.12	0.13	0.12	0.12	0.13	<0.01	<0.01	0.12	0.14	0.10	0.15	0.04	0.03
LOI 1000	1.24	0.90	1.00	0.91	0.94	1.30	0.84	0.66	0.90	1.58	1.34	1.36	1.98	3.04
Mg#	0.34	0.36	0.36	0.32	0.33	0.36	0.27	0.22	0.34	0.37	0.32	0.19	0.40	0.38
La	33.2	31.1	32.9	31.9	31.6	30.5	17.1	28.0	32.3	24.7	20.5	14.9	20.7	24.0
Ce	67.9	61.3	67.8	64.1	62.8	61.1	33.9	53.0	64.9	58.7	47.5	35.8	46.0	52.7
Pr	7.37	6.42	7.21	6.99	6.65	6.66	3.42	5.08	7.06	7.20	5.69	4.01	4.79	5.35
Nd	25.6	22.3	24.7	24.5	23.5	24.1	10.7	15.1	24.7	23.0	18.0	13.4	13.9	15.5
Sm	4.08	3.46	3.99	3.77	3.70	4.14	1.73	2.38	3.80	3.98	3.09	2.47	2.43	2.76
Eu	0.91	0.91	0.87	0.85	0.92	0.93	0.26	0.29	0.89	0.80	0.72	0.49	0.48	0.56
Gd	2.77	2.34	2.76	2.54	2.44	2.67	1.36	2.08	2.37	2.63	2.04	1.68	1.74	2.09
Tb	0.33	0.32	0.32	0.31	0.31	0.32	0.21	0.32	0.30	0.34	0.27	0.23	0.28	0.28
Dy	1.68	1.43	1.54	1.43	1.50	1.58	1.18	1.79	1.49	1.67	1.19	1.23	1.61	1.56
Ho	0.29	0.26	0.29	0.25	0.26	0.25	0.26	0.38	0.26	0.30	0.24	0.23	0.34	0.29
Er	0.81	0.72	0.77	0.64	0.69	0.66	0.82	1.36	0.71	0.83	0.60	0.66	1.02	0.83
Tm	0.12	0.10	0.11	0.09	0.10	0.09	0.15	0.25	0.10	0.12	0.10	0.10	0.17	0.13
Yb	0.66	0.64	0.66	0.59	0.66	0.63	1.07	1.75	0.62	0.76	0.56	0.67	1.21	0.87
Lu	0.11	0.11	0.11	0.09	0.10	0.10	0.19	0.34	0.10	0.12	0.10	0.10	0.20	0.15
Y	7.7	7.0	7.5	7.0	7.0	6.8	7.2	11.7	7.1	7.1	5.8	5.3	6.1	7.5
ΣREE	145.83	131.41	144.03	138.05	135.23	133.73	72.35	112.12	139.60	125.15	100.60	75.97	94.87	107.07
LREE	139.06	125.49	137.47	132.11	129.17	127.43	67.11	103.85	133.65	118.38	95.50	71.07	88.30	100.87
HREE	6.77	5.92	6.56	5.94	6.06	6.30	5.24	8.27	5.95	6.77	5.10	4.90	6.57	6.20
LREE/HREE	20.54	21.20	20.96	22.24	21.32	20.23	12.81	12.56	22.46	17.49	18.73	14.50	13.44	16.27
LaN/YbN	33.91	32.76	33.61	36.45	32.28	32.64	10.77	10.79	35.12	21.91	24.68	14.99	11.53	18.60
δEu	0.78	0.92	0.76	0.79	0.88	0.80	0.50	0.39	0.85	0.71	0.83	0.70	0.68	0.69
δCe	1.00	0.99	1.02	0.99	0.99	0.99	1.01	0.99	0.99	1.05	1.04	1.09	1.07	1.08

Table 2. *Cont.*

Sample No.	N1-Q1	N1-Q2	N1-Q3	N1-Q4	N1-Q5	N1-Q6	N2-Q1	N2-Q2	N2-Q3	N3-Q1	N3-Q2	N3-Q3	N3-Q4	N3-Q5
Rb	104.5	97.4	103.5	94.3	94.2	118.5	214	200	93.5	113.0	118.0	129.5	195.0	272
Ba	710	741	729	758	757	870	751	327	736	710	690	360	430	480
Th	11.50	7.71	12.10	8.94	8.25	8.98	33.1	37.7	8.45	6.58	6.59	16.45	32.1	36.2
U	4.89	3.09	3.87	5.63	4.64	2.69	6.63	16.10	3.75	1.7	2.8	8.0	8.1	20.2
K	29,100	31,100	31,300	31,100	29,500	33,000	52,000	47,900	28,500	32,900	33,200	33,100	44,400	56,700
Ta	0.96	0.69	0.80	0.71	0.84	0.58	1.82	2.23	0.69	0.36	0.55	0.64	1.11	0.85
Nb	9.2	7.9	9.2	8.6	8.5	7.6	4.2	9.0	7.7	4.7	6.9	5.5	4.2	3.8
Sr	551	575	578	571	604	529	175.0	134.0	574	488	399	79.4	125.0	119.0
P	630	590	610	550	550	590	20	30	560	600	480	620	170	160
Zr	196.0	183.0	190.0	190.0	193.0	195.0	82.9	85.6	168.0	178	158	66	79	79
Ti	1860	1850	1820	1840	1820	1800	260	430	1820	1400	1640	890	750	620

5.2. Zircon U–Pb Geochronology

Zircons from samples CAP-1, CAP-2, and CAP-3 are colorless or light brown, transparent and euhedral. Most of the zircons are 80–110 μm in length, with an aspect ratio of 1:1–3:1. Zircons generally have low CL brightness, obvious oscillation zone and dark rims (Figure 5), combined with a high Th/U ratio (0.38–1.25; Table 3), indicating a magmatic origin. The zircon U-Pb dating results are shown in Table 3. Except for individual data, most of the analysis results were nearly concordant (Figure 5). The monzogranite sample CAP-1, CAP-2, and CAP-3 yielded $^{206}Pb/^{238}U$ ages 172 to 178 Ma, 174 to 177 Ma, 165 to 181 Ma, with a weighted mean $^{206}Pb/^{238}U$ age 174.7 $\pm$ 1.3 Ma (n = 16, mean squared weighted deviation (MSWD) = 0.56); 174.9 $\pm$ 1.4 Ma (n = 12, MSWD = 0.19); 174.3 $\pm$ 1.8 Ma (n = 17, MSWD = 0.71), respectively (Figure 5). These zircon U–Pb ages of monzogranite are consistent with the molybdenite Re-Os isochron age of 167.3–168.7 Ma obtained by Song et al. (2016) [76]. The emplacement age of intrusions and the formation age of mineralization are close to each other and their sequence is reasonable, which suggest a causal relationship between mineralization and monzogranite intrusion.

5.3. Zircon Hf Isotopic

The Hf isotopic composition of 15 zircons from the CAP-1 of Chang'anpu monzogranite were analyzed at the same sites, with the U–Pb dating. The data were presented in Table 4. The initial $^{176}Hf/^{177}Hf$ ratio was corrected by the U–Pb age previously obtained. $^{176}Lu/^{177}Hf$ ratios of zircon range from 0.000520–0.000984. $\varepsilon_{Hf(t)}$ values range from +6.72 to +8.85 (t = 171 Ma); the average is +7.60. Two-stage Hf model ages (T_{DM2}) of zircons range from 551 to 673 Ma. All analysis results were plotted between the evolutionary reference lines of the Chondrite Uniform Reservoir (CHUR) and depleted mantle in the $\varepsilon_{Hf(t)}$ vs. age diagram (Figure 6; Table 3).
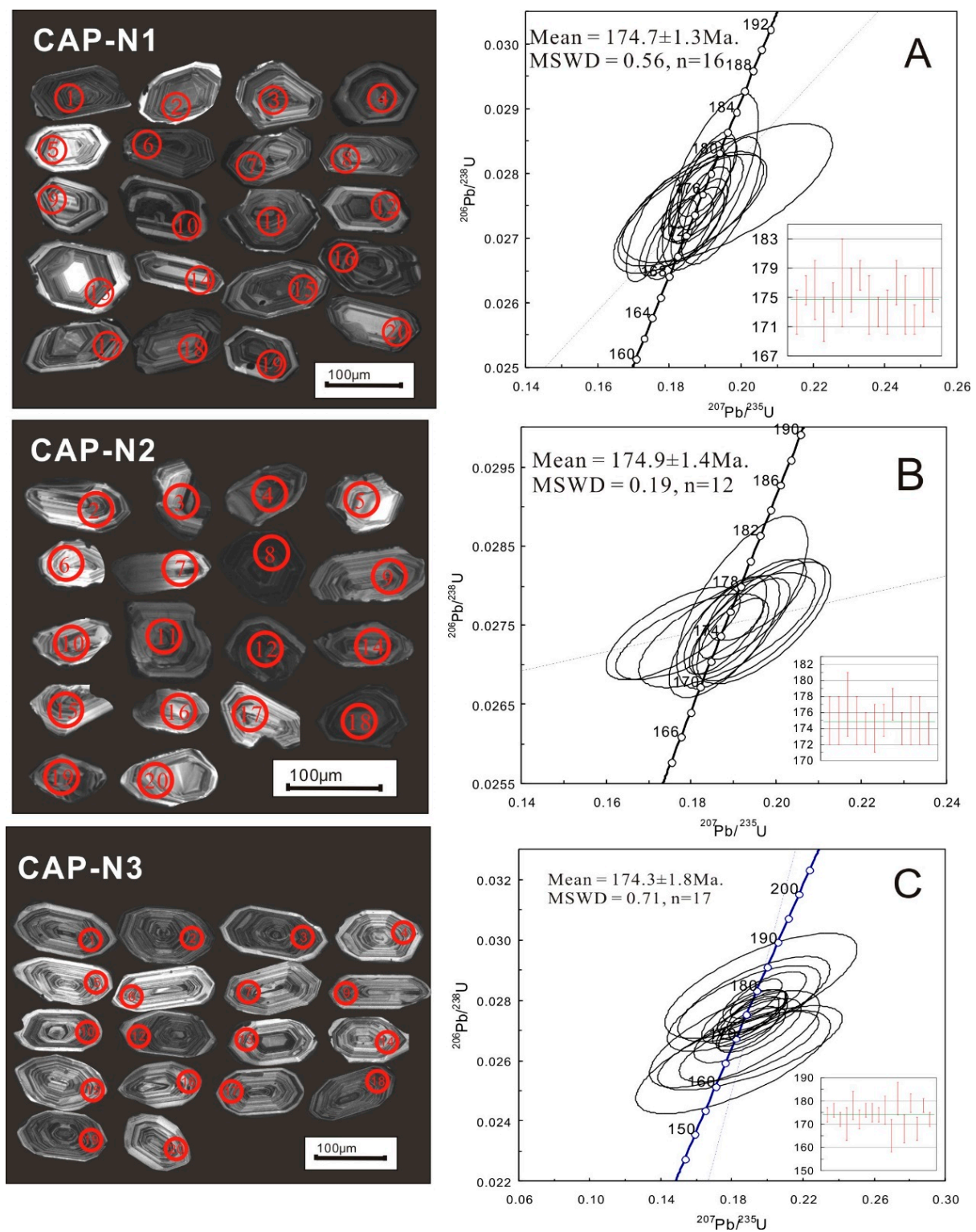
Figure 5. Cathodoluminescent images and LA-ICP-MS zircon U–Pb concordia diagrams for the monzogranite. (**A**) CAP-N1, (**B**) CAP-N2, (**C**) CAP-N3.

Table 3. Results of LA-ICPMS U–Pb dating for the single-grain zircon from the monzogranite.

Spot No.	Content (ppm)			Isotopic Ratios						Ages (Ma)			
	Th	U	Th/U	$^{207}Pb/^{206}Pb$	1σ	$^{207}Pb/^{235}U$	1σ	$^{206}Pb/^{238}U$	1σ	$^{207}Pb/^{235}U$	1σ	$^{206}Pb/^{238}U$	1σ
CAPN1-01	1166	1909	0.61	0.0505168	0.001	0.188312	0.0052	0.027276	0.0004	175	4	173	3
CAPN1-03	934	1157	0.81	0.0499482	0.002	0.188502	0.0057	0.027734	0.0004	175	5	176	2
CAPN1-05	885	1074	0.82	0.0528013	0.005	0.196195	0.0193	0.027704	0.0007	182	16	176	4
CAPN1-07	565	814	0.69	0.0494549	0.002	0.182835	0.0062	0.027033	0.0004	170	5	172	3
CAPN1-08	1256	2166	0.58	0.0499937	0.001	0.188835	0.0054	0.027514	0.0004	176	5	175	2
CAPN1-09	1295	1274	1.02	0.0507414	0.002	0.191476	0.0088	0.027871	0.0009	178	8	177	6
CAPN1-10	1794	4265	0.42	0.0494465	0.001	0.187614	0.0051	0.027709	0.0005	175	4	176	3
CAPN1-11	597	1330	0.45	0.0498194	0.001	0.190612	0.0055	0.027937	0.0004	177	5	178	2
CAPN1-12	915	1460	0.63	0.0504564	0.004	0.185356	0.0138	0.027401	0.0006	173	12	174	4
CAPN1-13	906	1309	0.69	0.0500006	0.002	0.185935	0.0062	0.027183	0.0004	173	5	173	2
CAPN1-14	1593	3157	0.5	0.0477714	0.001	0.175782	0.0051	0.02713	0.0005	164	4	173	3
CAPN1-15	1319	1912	0.69	0.049947	0.001	0.190564	0.0052	0.02789	0.0005	177	4	177	3
CAPN1-17	1514	2242	0.68	0.0515432	0.003	0.186514	0.0137	0.027435	0.0006	174	12	174	4
CAPN1-18	1221	1030	1.19	0.0487357	0.002	0.179784	0.0053	0.027008	0.0004	168	5	172	2
CAPN1-19	1724	3141	0.55	0.0497213	0.002	0.194386	0.0073	0.027577	0.0006	180	6	175	4
CAPN1-20	1025	949	1.08	0.0500614	0.002	0.189231	0.0075	0.027619	0.0004	176	6	176	3
CAPN2-02	416	659	0.63	0.0520146	0.003	0.197099	0.0104	0.027532	0.0005	183	9	175	3
CAPN2-03	528	634	0.83	0.0510265	0.002	0.195921	0.0104	0.02757	0.0005	182	9	175	3
CAPN2-05	556	833	0.67	0.0512714	0.002	0.192038	0.0101	0.027793	0.0007	178	9	177	4
CAPN2-06	699	1863	0.38	0.0495716	0.002	0.18808	0.0064	0.027496	0.0004	175	5	175	3
CAPN2-07	438	1062	0.41	0.0502362	0.002	0.188845	0.0062	0.027359	0.0003	176	5	174	2
CAPN2-08	701	861	0.81	0.0520615	0.003	0.187827	0.0086	0.027355	0.0005	175	7	174	3
CAPN2-09	820	882	0.93	0.0508521	0.002	0.192526	0.0071	0.027582	0.0003	179	6	175	2
CAPN2-12	406	768	0.53	0.0512003	0.002	0.195554	0.0076	0.027821	0.0003	181	6	177	2
CAPN2-14	490	822	0.6	0.0512211	0.006	0.179694	0.0115	0.027362	0.0004	168	10	174	2
CAPN2-15	556	641	0.87	0.0481857	0.003	0.188462	0.0137	0.027444	0.0005	175	12	175	3
CAPN2-20	697	1391	0.5	0.0461123	0.002	0.175779	0.0104	0.027403	0.0004	164	9	174	2
CAPN3-01	309	367	0.84	0.05053	0.004	0.18999	0.014	0.02728	0.0005	177	12	174	3
CAPN3-02	289	549	0.53	0.05109	0.003	0.19454	0.0112	0.02762	0.0005	180	10	176	3
CAPN3-03	1029	1110	0.93	0.05064	0.003	0.18893	0.0117	0.02706	0.0005	176	10	172	3
CAPN3-04	396	416	0.95	0.04931	0.009	0.18155	0.0316	0.02671	0.0011	169	27	170	7
CAPN3-05	158	263	0.6	0.04978	0.008	0.19239	0.0282	0.02804	0.0009	179	24	178	6
CAPN3-06	238	291	0.82	0.05078	0.006	0.18888	0.02	0.02699	0.0007	176	17	172	4
CAPN3-07	247	324	0.76	0.05019	0.003	0.19099	0.0127	0.02761	0.0005	177	11	176	3
CAPN3-10	519	689	0.75	0.04934	0.004	0.18679	0.0158	0.02747	0.0006	174	13	175	4

Table 3. *Cont.*

Spot No.	Content (ppm)			Isotopic Ratios						Ages (Ma)			
	Th	U	Th/U	^{207}Pb/^{206}Pb	1σ	^{207}Pb/^{235}U	1σ	^{206}Pb/^{238}U	1σ	^{207}Pb/^{235}U	1σ	^{206}Pb/^{238}U	1σ
CAPN3-12	819	1036	0.79	0.05026	0.003	0.18991	0.011	0.02742	0.0005	177	9	174	3
CAPN3-13	163	328	0.5	0.04892	0.008	0.18685	0.0284	0.02773	0.0009	174	24	176	6
CAPN3-14	114	194	0.59	0.05055	0.01	0.18068	0.0361	0.02595	0.0011	169	31	165	7
CAPN3-15	238	238	1	0.05008	0.009	0.19644	0.0357	0.02848	0.0012	182	30	181	7
CAPN3-16	321	302	1.07	0.05229	0.01	0.19021	0.0342	0.02642	0.0009	177	29	168	6
CAPN3-17	424	386	1.1	0.05125	0.004	0.19832	0.0155	0.0281	0.0006	184	13	179	4
CAPN3-18	378	535	0.71	0.05205	0.007	0.18961	0.0259	0.02646	0.0008	176	22	168	5
CAPN3-19	1015	809	1.25	0.05018	0.003	0.19373	0.0095	0.02805	0.0004	180	8	178	3
CAPN3-20	1111	458	2.42	0.05144	0.003	0.19129	0.0124	0.02702	0.0005	178	11	172	3

Table 4. Zircon Hf isotopic compositions for monzogranite in the Chang'anpu Mo deposit.

Spot No.	t (Ma)	$^{176}Yb/^{177}Hf$	$^{176}Lu/^{177}Hf$	$^{176}Hf/^{177}Hf$	$\pm2\sigma$	$\varepsilon_{Hf}(0)$	$\varepsilon_{Hf}(t)$	$T_{DM1}(Hf)$	$T_{DM2}(Hf)$	$f_{Lu/Hf}$
CAP1-1	168	0.02592766	0.0009840158	0.2828861	0.0000219	4.04	7.62	518	618	−0.97
CAP1-2	179	0.01729984	0.0006920099	0.2828532	0.0000187	2.87	6.72	561	673	−0.98
CAP1-3	175	0.01901383	0.0007703959	0.2828679	0.0000155	3.39	7.15	541	648	−0.98
CAP1-4	165	0.01363266	0.0005199855	0.2829033	0.0000164	4.64	8.21	488	585	−0.98
CAP1-5	176	0.01551419	0.0005905786	0.2828648	0.0000210	3.28	7.08	543	652	−0.98
CAP1-6	163	0.01858129	0.0006998950	0.2829231	0.0000192	5.34	8.85	462	551	−0.98

Note: $\varepsilon_{Hf}(t) = \{[(^{176}Hf/^{177}Hf) - (^{176}Lu/^{177}Hf) \times (e^{\lambda t}-1)]/[(^{176}Hf/^{177}Hf)CHUR(0) - (^{176}Lu/^{177}Hf)CHUR \times (e^{\lambda t}-1)] - 1\} \times 10,000.$ $(^{176}Hf/^{177}Hf)CHUR(0) = 0.282772$ and $(^{176}Lu/^{177}Hf)CHUR = 0.0332$ (Blichert-Toft and Albarède, 1997); $\lambda_{Lu} = 1.867 \times 10^{-11}$ year^{-1} [77].
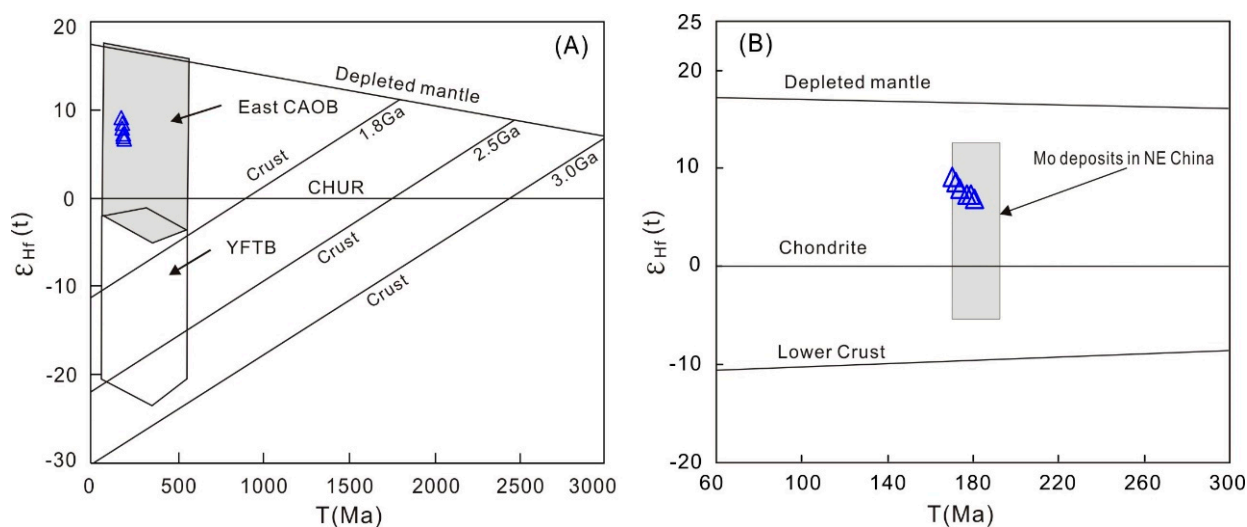
Figure 6. Zircon Hf isotopic characteristics of monzogranite. CHUR: bulk earth chondritic uniform reservoir. (**A**) The characteristic of Hf isotopic composition, (**B**) $\varepsilon_{Hf}(t)$ versus T (Ma) diagram of Mo deposits in NE China.

6. Discussion

6.1. Petrogenesis and Sources of the Monzogranite Intrusion

6.1.1. Genetic Type of the Monzogranite

The genetic types of granitic can reflect the tectonic setting and source of magmatic rocks [78–81], which can genetically be divided into I-, S-, A-, and M- types [82–85]. The Chang'anpu monzogranite can be excluded as M-type granite, firstly because M-type granite has high Na/K (>1) and is mainly composed of plagioclase [42]. Many studies have shown that the content of P_2O_5 is negatively correlated with SiO_2 in I-type, while P_2O_5 increases or remains unchanged with the increase of SiO_2 in S-type [86,87]. The P_2O_5 content of monzogranite in Chang'anpu deposit ranges from 0.01% to 0.15%, and is negatively correlated with SiO_2 (Figure 7G). In general, A/CNK = 1.1 can be used as a boundary between S-type and I-type, while peraluminous granites are generally believed to be S-type [82]. The Chang'anpu monzogranite were weaky peraluminous with A/CNK < 1.1 (0.96–1.07). These two points show that the monzogranite is not S-type. Generally, alkaline dark minerals are common in A-type granite, which are enriched in REE, Nb, Y, and other high field strength elements (HFSE), while depleted in Eu, Ba, and Sr. However, the content of mafic alkaline minerals in monzogranite is very low, and Nb, Ta, Ti, and Y elements are not enriched. Furthermore, the content of (Zr + Nb + Ce + Y) in samples ranged from 112.6 to 280.8 ppm, which was lower than that of A-type (≥350 ppm). Thus, Chang'anpu monzogranite is not an A-type, but an I-type.
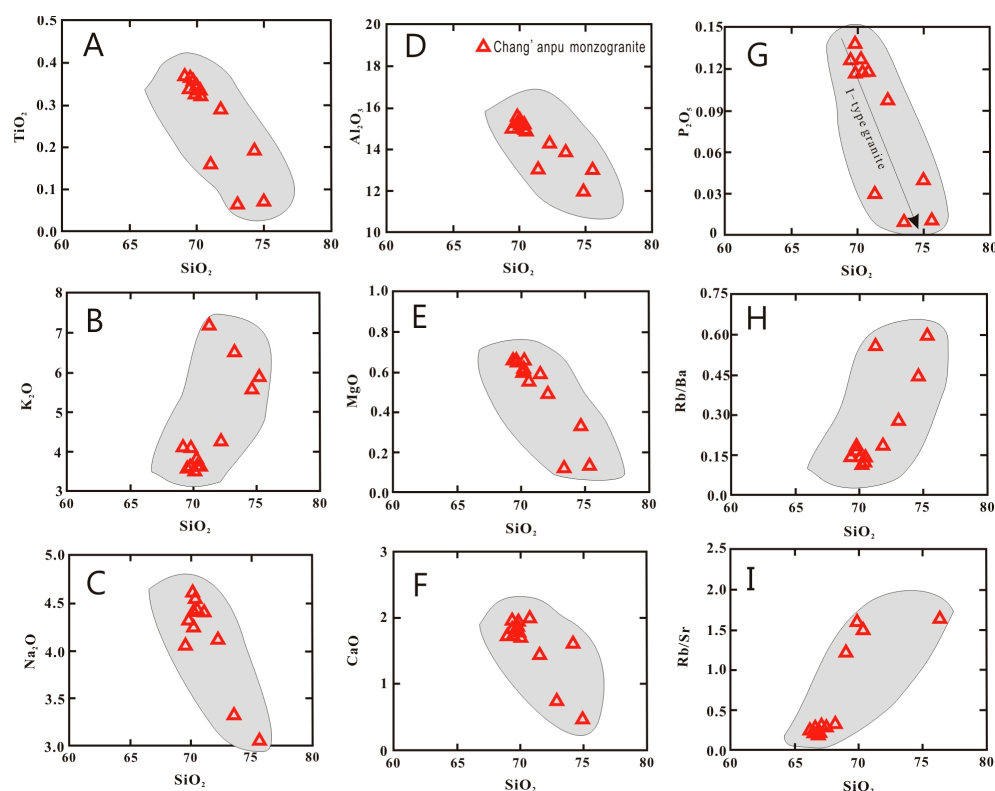
Figure 7. Harker variation diagrams for the monzogranite. TiO_2 (**A**), K_2O (**B**), Na_2O (**C**), Al_2O_3 (**D**), MgO (**E**), CaO (**F**), P_2O_5 (**G**), Rb/Ba (**H**), and Rb/Sr (**I**) versus SiO_2 diagrams.

Except for the N3-Q3 sample with abnormally high SiO_2 content (84.39%) due to silicification alteration, the SiO_2 in Figure 7A–G shows a linear correlation with other elements, indicating that the magma contains a certain content of differentiated minerals, such as feldspar and hornblende [88]. The data obtained from monzogranite samples show alkali rich and relatively high silica content (maximum 84.39%, most 69.50%–75.42%), with a high differentiation index (86–96) and the depletion of P, Nb, Ti and Eu elements in the samples indicating that the rock has undergone crystallization fractionation during magma evolution. The fractional crystallization of plagioclase and K-feldspar causes negative Eu anomalies, while the separation of Ti-bearing minerals and apatite usually results in the depletion of Nb, Ti, and P. It is well known that in the process of magmatic fractionation crystallization, Ba and Sr are enriched in plagioclase, while Rb tends to residual magma, making it possible to trace the fractional crystallization by Rb/Ba and Rb/Sr ratios [42]. The contents of Sr and Ba show they are negatively correlated with SiO_2, whereas Rb/Ba and Rb/Sr are positively correlated with SiO_2 (Figure 7H,I), indicating that monzogranite was formed by fractional crystallization. Data from samples in the Th/Ti vs. Th diagram define a curving array [89] (Figure 8A), and are distributed along the fractional crystallization line in the La/Sm vs. La diagram (Figure 8B). Fractional crystallization and partial melting may be regarded as antipathetic and seemingly reversible processes, their manifestation in the Earth's crust leads to markedly different outcomes; large volumes of peraluminous melt is formed during partial melting, while limited volumes of peraluminous melt is formed during fractional crystallization. Although fractional crystallization was the dominant controlling factor for the evolution of monzogranite, the existence of a large amount of peraluminous I-type melt from Archaean through to the present indicates that partial melting plays an important role in the long-term evolution of the crust [90]. In SiO_2 vs. K_2O diagram (Figure 8C), samples plot in high-K calc-alkaline field and are weakly peraluminous (Figure 8D). Based on the above, it suggests that the Chang'anpu monzogranite intrusion have been subjected to significant fractional crystallization, belong to high-K

calc-alkaline highly fractionated I-type granite. Monzogranite exhibited high SiO_2 and Sr, relatively lower MgO, Y, Yb content and high Sr/Y ratio, and weak Eu anomaly, indicating that it has the attributes of adakite. On the Sr/Y − Y discriminant diagram (Figure 9), except for a few samples, most samples fall into the adakite area [21,91–93], indicating that monzogranite belongs to adakite rock.
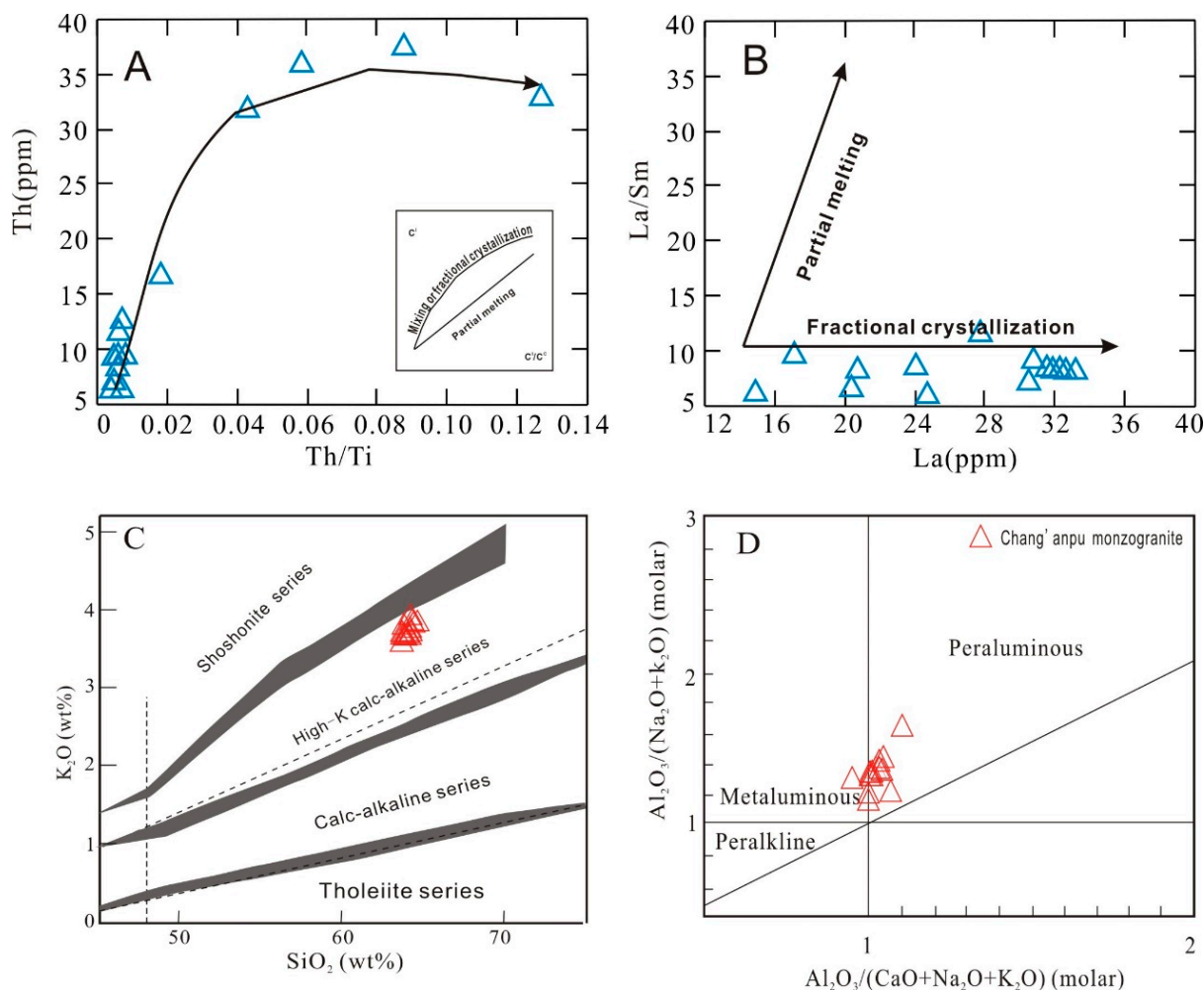

Figure 8. Petrogenetic diagrams for the monzogranite. (**A**) Th vs. Th/Ti diagram (Schiano et al., 2010) [89]. (**B**) La/Sm vs. La diagram [94]. The inset is aschematic C^I versus C^I/C^C diagram (C^I, incompatible element concentration, and C^C, compatible element concentrations). (**C**) Diagrams of SiO_2 vs. K_2O. (**D**) A/CNK vs. A/NK. The boundary lines in the SiO_2 vs. K_2O and A/CNK vs. A/NK diagrams are from Peccerillo and Taylor (1976), and Maniar and Piccoli (1989) [95,96], respectively. The symbols are the same as in Figure 7.

6.1.2. Petrogenesis and Source of the Magma

As a common accessory mineral in granites, zircon is often used to identify the source of magma [68,97,98]. The value of $^{176}Hf/^{177}Hf$ varies greatly among zircons from different magmatic sources. The Lu-Hf fractionation results in high Lu/Hf ratios in mantle residue, but low Lu/Hf ratios in basaltic magmas during partial melting. The depleted mantle usually has positive radiogenic $\varepsilon_{Hf(t)}$ values, while the enriched mantle, ancient crust show negative $\varepsilon_{Hf(t)}$ values. The magma derived from the juvenile crust usually has a positive $\varepsilon_{Hf(t)}$ value as it has not had enough time to be derived from depleted mantle. To summarize, chondrites, depleted mantle, and juvenile crust have a high $^{176}Hf/^{177}Hf$ ratio,

which is usually positive, while the $^{176}Hf/^{177}Hf$ ratio is relatively low, and often negative, in enriched mantle and pre-existing crust.
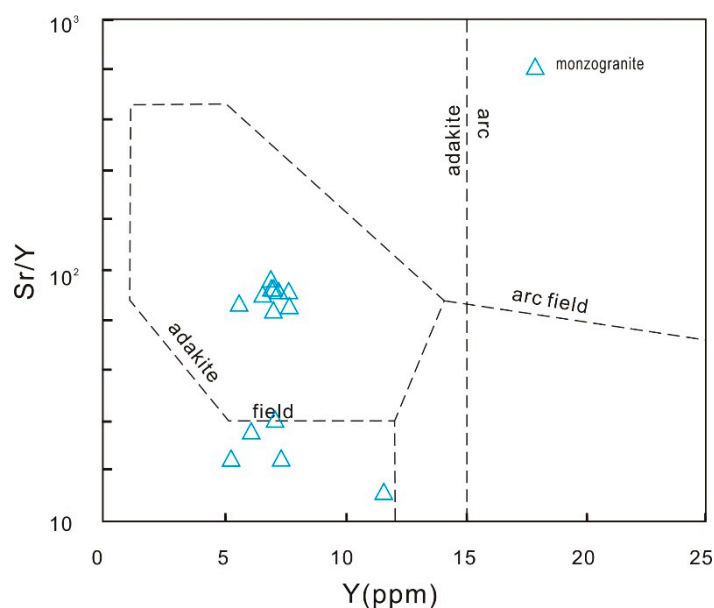

Figure 9. Variations of Sr/Y versus Y (ppm) in monzogranite associated with Chang'anpu porphyry Mo deposit (adapted from Kepezhinskas al., 2022) [21].

The monzogranite of the Chang'anpu deposit contain zircons with the $^{206}Pb/^{238}U$ ages 163 to 179 Ma, the $\varepsilon_{Hf(t)}$ values of +6.72 to +8.85, and the T_{DM2} ages range from 551 to 673 Ma, plot between the evolutionary reference lines of the CHUR and depleted mantle (Figure 6). However, granite derived directly from mantle can be ruled out, as few granites distributed in this area have mantle-source characteristics [23]. This indicates that lower crust materials derived from Mesoproterozoic depleted mantle, or subducted slab, may had contributed to the magmatic source. Similar to the most porphyry deposits in the Lesser Khingan Mountains–Zhangguangcai Mountains, Chang'anpu Mo deposits have $\delta^{34}S$ values broadly consistent with those of mantle magma (0‰ ± 3‰). The Pb content is a mixture of the Pb from mantle-derived magma and the radiogenic Pb from country rocks [22,37,38]. Both of the S-Pb isotope compositions are similar to subduction zone magmatism, indicating that the diagenetic and ore-forming materials have a mixed source of crust and mantle. Wu et al. (2000) [42] pointed out that the magmatic sources of Mesozoic granites in NE China usually involve juvenile lower crustal materials that have been partial melted, and are characterized by positive $\varepsilon_{Nd(t)}$ value, low $^{87}Sr/^{86}Sr$ ratio, and younger Nd model age. Comparing Chang'anpu monzogranite with other Mesozoic granites in NE China, most of them have positive $\varepsilon_{Hf(t)}$ values and younger T_{DM} ages, which proves that crust beneath NE China had a significant growth episode during the Meso-Neoproterozoic age, and also indicating their source was depleted mantle or subducted slab [23,24]. In conclusion, the monzogranite in Chang'anpu deposit has the same source and tectonic setting as other porphyry deposits distributed in Lesser Khingan Mountains–Zhangguangcai Mountains; the partial melting and subsequent fractional crystallization of the juvenile lower crust derived from Mesoproterozoic depleted mantle, or subducted slab, played a key role in the formation of the monzogranite intrusion.

6.2. Temporal and Spatial Distribution of Regional Metallogenic Granitic Intrusions

Zircon U-Pb dating shows that ore-forming granites in the Lesser Khingan Mountains-Zhangguangcai Mountains were mainly formed in the early-middle Jurassic-late early Cretaceous: the Luming monzogranite (197.1 ± 1.6 Ma) and monzogranite porphyry (183.2 ± 1.9 Ma) were formed in the early Jurassic, and mineralization is mainly related to

late monzogranite porphyry; the Fu'anpu porphyritic monzogranite (166.9 ± 6.7 Ma) and dark microgranular enclave (quartz diorite) (168.6 ± 1.9 Ma) were formed in the middle Jurassic; both Jidetun monzogranite (170.8 ± 1.9 Ma) and granodiorite (180.2 ± 0.8 Ma) were formed in the middle Jurassic; the Baoshan granodiorite (164.4 ± 1.9 Ma) and quartz diorite (165.2 ± 1.7 Ma) were formed in the middle Jurassic; the age of the Kanchuangou granodiorite is 111.8 ± 1.4 Ma, which was formed in the late early Cretaceous; and the Chang'anpu monzogranite (174.3 ± 1.8 Ma −174.9 ± 1.4 Ma) was formed in the middle Jurassic (this study). Based on published data and the results of this study, it is found that the ore-forming granites in the early Jurassic are mainly distributed in the Lesser Hinggan Mountains and the Northern Yanbian area, and are mostly monzonite (porphyry)-granodiorite-quartz monzonite. The ore-forming granites of middle Jurassic are mainly distributed in the Zhangguangcai Mountains and Southern Yanbian, and the lithology is monzonitic-granodiorite (porphyry). Early-middle Jurassic granites are the most widely distributed and longest lasting magmatic activity in the region; most ore-forming rocks of the deposit were formed in this period. In spatial morphology, it is distributed in a NNE direction and often occurs as batholith, stock, and compound rock mass. The rock types are mainly calc-alkaline and high-K calc-alkaline monzogranite-granodiorite, which is considered to be the product of the subduction of the Pacific plate beneath the Eurasian continent [47,99].

6.3. Diagenetic and Metallogenic Model

In the early Jurassic, the Pacific Ocean plate subducted beneath the Eurasian continental plate, and continuous subduction resulted in the regional compression environment, thickening of the continental crust, partial melting of the thickened lower crust material and dehydration and melting of the subducted slab-formed mineral-rich granitic magma. Under the compression environment, magma cannot easily pass directly through the upper crust to form volcanic rocks, and can only continuously accumulate to form a larger magma chamber, which accumulates more crust-derived ore-forming materials [100]. Magma in the shallow magma chamber was unable to erupt and began fractional crystallization during evolution under pressure, forming porphyry [3,101,102]. As molybdenum is an incompatible element, the continuous evolution of crystallization and fractionation resulted in the enrichment of molybdenum in the late residual magma melt. When the magma is deeply emplaced, pressure is higher and the solubility of volatiles increases correspondingly, no boiling occurs at the beginning of emplacement, and no independent fluid phase is formed. With the slow evolution of magma to the late stage, volatiles are saturated, forming large-scale low-medium salinity supercritical fluid under high fluid pressure [103–105]. The ore bearing fluid is exsolved from the magma chamber, immiscibility leads to phase separation of the fluid, and boiling causes large-scale molybdenum precipitation, forming large-scale porphyry molybdenum deposits related to plutonic intrusions represented by Daheishan, Luming, Chang'anpu, Fu'anpu, and Jidetun, etc. From the perspective of the formation and evolution of porphyry molybdenum deposit, the compressive tectonic environment is more conducive to plutonic magma in forming porphyry in the shallow part, providing space and pressure conditions for the evolution of molybdenum-bearing melt, and the accumulation and precipitation of molybdenum elements.

6.4. Geodynamic Setting

Numerous Jurassic porphyry molybdenum deposits have been discovered and mined in NE China over the last few years; however, there is still some controversy overtheir tectonic setting. Some researchers attribute metallogenesis to basin-and range tectonic setting [106]; closure of the Asian ocean [107]; and the mantle plume model [108], whereas others believe that the post-orogenic extension is the metallogenic tectonic setting [109]. The samples of Chang'anpu monzogranite is characterized by enriched LILEs and incompatible elements, but relatively depleted in HFSEs, which conforms to the granitic magmas that derived from the active continental margin tectonic setting that have undergone extensive

fractional crystallization during evolution. All samples plotted in the volcanic arc and syn-collision field in Nb-Y and Rb- (Y + Nb) discrimination diagrams suggesting an active continental margin setting (Figure 10A,B). Similarly, the monzogranite samples show a continental arc setting in the Zr/Al_2O_3 versus TiO_2/Al_2O_3, and Ce/P_2O_5 versus Zr/TiO_2 discrimination diagrams (Figure 10C,D). The Th/Ta ratio of sample ranges from 10.9 to 21.1 belongs to the active continental margin igneous rocks [42]. By comparing the tectonic setting of giant porphyry deposits around the world, it shows that the subduction-related island- and continental-arc settings are relatively common tectonic settings for most porphyry deposits [47]. Most of the worldwide porphyry deposits occur in active convergent plate boundaries, and Mesozoic-Cenozoic orogenic belts with subduction-related tectonic setting [3,4]. The models of adakite petrogenesis include the melting of thickened and delaminated mafic lower crust, basalt underplating of the continental crust, and high-pressure fractionation (amphibole-garnet) of mantle-derived, hydrous mafic melts [91]. As the Chang'anpu monzogranite intrusion was developed in a continental arc setting, we suggest that the adakites were related to the oceanic slab melting and then being producing through the northeastward subduction of the Paleo-Pacific ocean crust, beneath the continental terranes in Eastern China in the Jurassic.
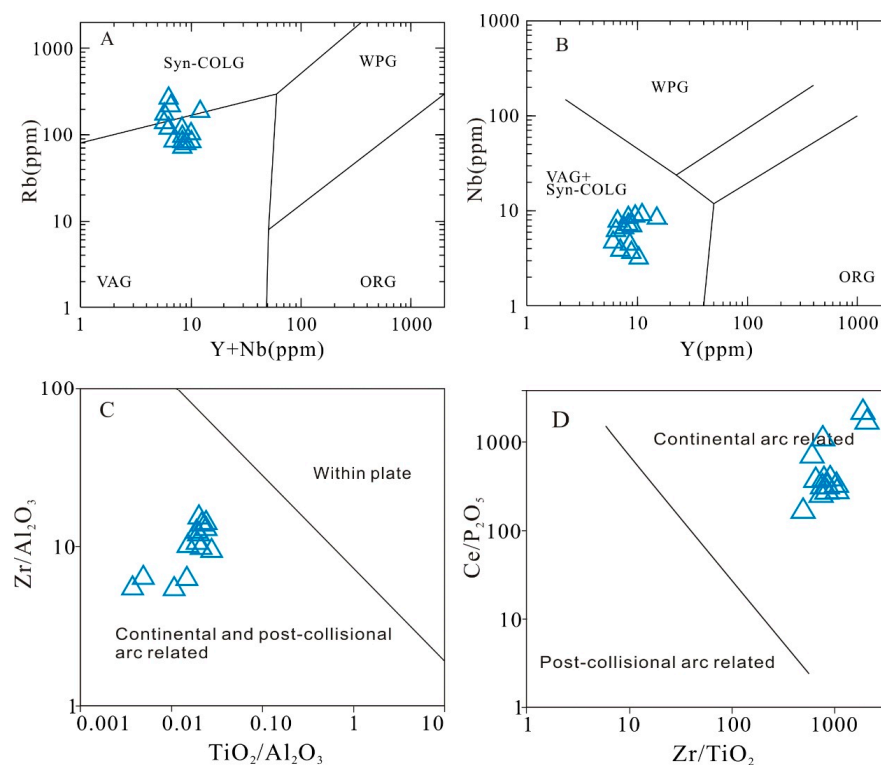
Figure 10. (**A**) Rb– (Y + Nb), (**B**) Nb–Y, (**C**) Zr/Al_2O_3—TiO_2/Al_2O_3 and (**D**) Ce/P_2O_5—Zr/TiO_2 discrimination diagrams of the monzogranite (adapted from Pearce et al., 1984; Muller and Groves, 1994; Pearce, 1996) [78,110,111]. VAG: volcanic arc granites; ORG: ocean ridge granites; WPG: within-plate granites; syn-COLG: syn-collision granites; post-COLG: post-collision granites. The symbols are the same as in Figure 7.

The Eastern part of China underwent Circum-Pacific tectonics to varying degrees, and NE China suffered from the subduction of Paleo-Pacific since the Jurassic [112]. The initial subduction time of Pacific plate was determined by Dongning-Wangqing-Hunchun calc-alkaline volcanic associations, which was found in the Heilongjiang-Jilin area, with ages of 173 to 190 Ma [47]. The deformation age of Heilongjiang complex also provides key markers for the duration of the subduction of Paleo-Pacific plate in Early Jurassic. According to [113] the westward subduction of Pacific plate had already affected Lesser Khingan Mountains-Zhangguangcai Mountains in the Early Jurassic by analyzing the

geochronology and geochemistry data of granitoids. The NNE direction distribution of Jurassic granitoids in the Lesser Khingan Mountains-Zhangguangcai Mountains also suggests that the early Yanshanian large-scale diagenesis and mineralization should be related to the subduction of the Pacific plate; the subduction also formed a tectonic transition period conducive to the formation of porphyry deposits [6,42,47,114]. By comparing the geotectonic background of the Lesser Khingan Mountains-Zhangguangcai Mountains in the Early-Middle Jurassic, and Early Cretaceous, it can be found that the region was mainly under the background of lithospheric compression related to the subduction of the Pacific plate in Early-Middle Jurassic. In the region, granites are distributed in a NNE direction, and often occurs as batholith, stock, and compound rock mass, with rock types mainly being calc-alkaline and high-K calc-alkaline monzogranite- granodiorite, suggesting that its formation may be related to the continuous subduction of the Pacific plate [46,99]. In addition, the molybdenum deposits formed are mainly of stock and fine-vein type, related to plutonic intrusions. The geodynamic in Early Cretaceous for this region, and in Eastern China, is that continental breakup and rapid plate motion, including Pacific plate subduction, resulted in large scale lithospheric delamination, leading to a mantle avalanche, asthenosphere upwelling, and subsequent crustal melting in an extensional setting [115], forming mainly porphyry type and hydrothermal vein type copper gold deposits. From the above diagenetic and metallogenic mechanism, plutonic magmatism under a compression environment is more conducive to the formation and evolution of porphyry bodies and the migration, accumulation and precipitation of molybdenum elements, to form molybdenum ore bodies. Therefore, most of the porphyry Mo deposits in China were formed under the compression background of the Early-Middle Jurassic. The subduction of the Pacific plate in the Early-Middle Jurassic thickened the lithosphere, which accelerated the interaction between crust-mantle materials. The ocean crust subducted to a certain depth and began to dehydrate, then removed CO_2, which, as it left the ocean crust, accelerated the partial melting of the lithospheric mantle to form basaltic magma. The underplating of basaltic magma melted the crust and formed ore-bearing granitic magma, which is the reason magma in the Early-Middle Jurassic has the characteristics of crust-mantle mixed source. In conclusion, we consider that the formation of the monzogranite intrusion and Chang'anpu deposit was closely related to the westward subduction of Pacific plate beneath Eurasian Plate, in Early-Middle Jurassic. During the same geological period, the subduction-related magmatism also formed a series of non-ferrous deposits in Eastern China (Figure 11).
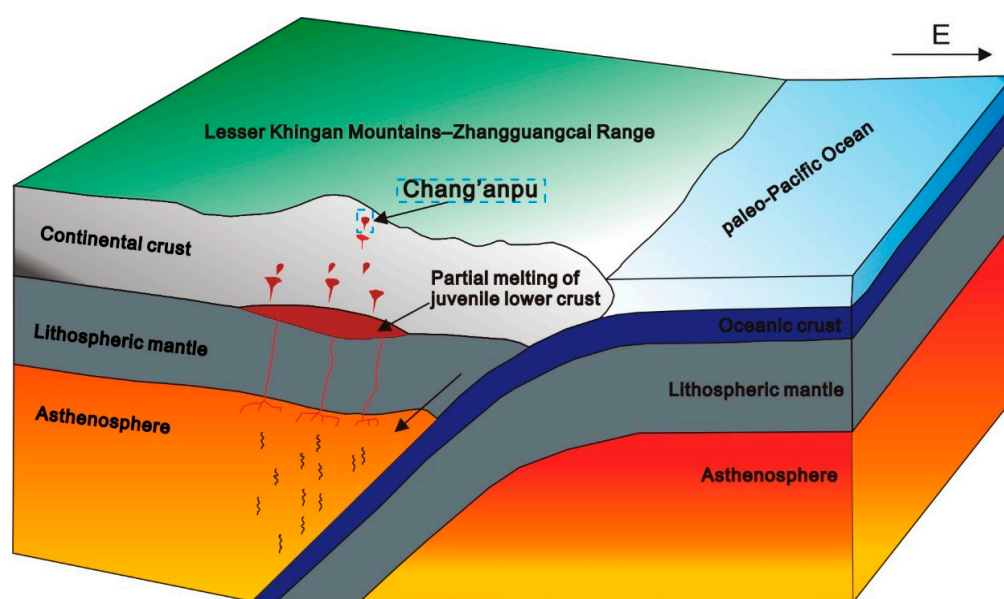

Figure 11. Diagenetic and metallogenic model of Early–Middle Jurassic porphyry deposit (modified after Guo et al. (2015) [116].

7. Conclusions

1. LA–ICP–MS zircon U–Pb dating reveals that the emplacement age of monzogranite intrusions in the Chang'anpu Mo deposit was 174.3 ± 1.8 to 174.9 ± 1.4 Ma. The emplacement age of intrusions, and the formation age of mineralization (168.0 ± 1.0 Ma), are close to each other and their sequence is reasonable, which suggests the causal relationship between mineralization and monzogranite intrusion.

2. The Chang'anpu monzogranite intrusion has been subjected to significant fractional crystallization, belonging to high-K calc-alkaline highly fractionated I-type granite.

3. Positive $\varepsilon_{Hf(t)}$ values (6.72–8.85) and young T_{DM2} (551–673 Ma) of monzogranite indicate that the formation of intrusion and deposit are related to the partial melting, and subsequent fractional crystallization, of the juvenile lower crust derived from Mesoproterozoic depleted mantle.

4. Formation of the monzogranite intrusion and Chang'anpu deposit was closely related to the magmatism triggered by the westward subduction of Pacific plate beneath Eurasian Plate, in Early-Middle Jurassic.

References

1. Cooke, D.R.; Hollings, P.; Walshe, J.L. Giant porphyry deposits: Characteristics, distribution, and tectonic controls. *Econ. Geol.* **2005**, *100*, 801–818. [CrossRef]
2. Goldfarb, R.J.; Groves, D.I.; Gardoll, S. Orogenic gold and geological time: A global synthesis. *Ore Geol. Rev.* **2001**, *18*, 1–75. [CrossRef]
3. Sillitoe, R.H. A plate tectonic model for the origin of porphyry copper deposits. *Econ. Geol.* **1972**, *67*, 184–197. [CrossRef]
4. Sillitoe, R.H. Characteristics and controls of the largest porphyry copper-gold and epithermal gold deposits in the circum-Pacific region. *Aust. J. Earth Sci.* **1997**, *44*, 373–388. [CrossRef]
5. Kerrich, R.; Goldfarb, R.; Groves, D.; Garwin, S.; Jia, Y.F. The characteristics, origins and geodynamic settings of supergiant gold metallogenic provinces. *Sci. China Ser.* **2000**, *43*, 1–68. [CrossRef]
6. Mitchell, A.H.G. Metallogenic belts and angle of dip of Benioff zones. *Nature* **1973**, *245*, 49–52. [CrossRef]
7. He, X.H.; Deng, X.H.; Pirajno, F.; Zhang, J.; Li, C.; Chen, S.B.; Sun, H.W. The genesis of the granitic rocks associated with the Mo-mineralization at the Hongling deposit, eastern Tianshan, NW China: Constraints from geology, geochronology, geochemistry, and Sr-Nd-Hf isotopes. *Ore Geol. Rev.* **2022**, *146*, 104947. [CrossRef]
8. Li, J.; Li, C.-Y.; Liang, J.-L.; Song, M.-C.; Zhang, L.-P.; Song, Y.-X. Mineralization of the Shangjiazhuang Mo deposit in the Jiaodong peninsula, China: Constraints from S–H–O isotopes and fluid inclusions. *Solid Earth Sci.* **2021**, *6*, 370–384. [CrossRef]
9. Hou, X.-G.; Sun, D.-Y.; Gou, J.; Yang, D.-G. The origin of variable-delta 18O zircons in Jurassic and Cretaceous Mo-bearing granitoids in the eastern Xing-Meng Orogenic Belt, Northeast China. *Int. Geol. Rev.* **2019**, *61*, 129–149. [CrossRef]
10. Guo, X.; Zhou, T.; Jia, Q.; Li, J.; Kong, H. Highly differentiated felsic granites linked to Mo mineralization in the East Kunlun Orogenic Belt, NW China: Constrains from geochemistry, and Sr-Nd-Hf isotopes of the Duolongqiarou porphyry Mo deposit. *Ore Geol. Rev.* **2022**, *145*, 104891. [CrossRef]
11. Gao, Y.; Yang, Y.-C.; Han, S.-J.; Meng, F. Geochemistry of zircon and apatite from the Mo ore-forming granites in the Dabie Mo belt, East China: Implications for petrogenesis and mineralization. *Ore Geol. Rev.* **2020**, *126*, 103733. [CrossRef]

12. Shen, P.; Hattori, K.; Pan, H.D. Oxidation Condition and Metal Fertility of Granitic Magmas: Zircon Trace-Element Data from Porphyry Cu Deposits in the Central Asian Orogenic Belt. *Econ. Geol.* **2016**, *110*, 1861–1878. [CrossRef]

13. Mi, K.; Lü, Z.; Yan, T.; Yao, X.; Ma, Y.; Lin, C. Zircon geochronological and geochemical study of the Baogaigou Tin deposits, southern Great Xing'an Range, Northeast China: Implications for the timing of mineralization and ore genesis. *Geol. J.* **2020**, *55*, 5062–5081. [CrossRef]

14. Mi, K.-F.; Lü, Z.-C.; Yan, T.-J.; Zhao, S.-J.; Yu, H.-Y. SHRIMP U-Pb zircon geochronology and Hf isotope analyses of Middle Permian-Early Triassic intrusions in southern Manzhouli area, Northeast China: Implications for the subduction of Mongol-Okhotsk plate beneath the Erguna massif. *Int. Geol. Rev.* **2020**, *62*, 549–567. [CrossRef]

15. Wan, L.; Lu, C.; Zeng, Z.; Mohammed, A.S.; Liu, Z.; Dai, Q.; Chen, K. Nature and significance of the late Mesozoic granitoids in the southern Great Xing'an range, eastern Central Asian Orogenic Belt. *Int. Geol. Rev.* **2019**, *61*, 584–606. [CrossRef]

16. Chen, P.; Liu, B.; Long, Z.; Zhou, L.; Fu, Y.; Zeng, Q. Ore genesis of the Sadaigoumen porphyry Mo deposit, North China Craton: Constraints from pyrite trace element and lead isotope analyses. *Ore Geol. Rev.* **2022**, *142*, 104698. [CrossRef]

17. Cao, M.; Qin, K.; Li, G.; Evans, N.; Hollings, P.; Jin, L. Genesis of ilmenite-series I-type granitoids at the Baogutu reduced porphyry Cu deposit, western Junggar, NW-China. *Lithos* **2016**, *246–247*, 13–30. [CrossRef]

18. Zhang, X.-Z.; Wang, Q.; Dong, Y.-S. High-pressure granulite facies overprinting during the exhumation of eclogites in the Bangong-Nujiang suture zone, central Tibet: Link to flat-slab subduction. *Tectonics* **2017**, *36*, 2918–2935. [CrossRef]

19. Zhai, D.; Liu, J.; Tombros, S.; Williams-Jones, A.E. The genesis of the Hashitu porphyry molybdenum deposit, Inner Mongolia, NE China: Constraints from mineralogical, fluid inclusion, and multiple isotope (H, O, S, Mo, Pb) studies. *Miner. Depos.* **2018**, *53*, 377–397. [CrossRef]

20. Zheng, S.-H.; Gu, X.-X.; Zhang, Y.-M.; Wang, J.-L.; Peng, Y.-W.; Xu, J.-C.; Lv, X. Temporal and spatial separation mechanisms of the Cu and Mo mineralization in the Dabate porphyry deposit, Western Tianshan, Xinjiang, China. *Ore Geol. Rev.* **2022**, *146*, 104924. [CrossRef]

21. Kepezhinskas, P.; Berdnikov, N.; Kepezhinskas, N.; Konovalova, N. Adakites, high-Nb basalts and copper-gold deposits in magmatic arcs and collisional orogens: An overview. *Geosciences* **2022**, *12*, 29. [CrossRef]

22. Guo, Y.; Zeng, Q.; Yang, J.; Guo, F.; Guo, W.; Liu, J. Zircon U-Pb geochronology and geochemistry of Early-Middle Jurassic intrusions in the Daheishan ore district, NE China: Petrogenesis and implications for Mo mineralization. *J. Asian Earth Sci.* **2018**, *165*, 59–78. [CrossRef]

23. Zhou, L.-L.; Zeng, Q.-D.; Liu, J.-M.; Friis, H.; Zhang, Z.-L.; Duan, X.-X. Geochronology of the Xingshan molybdenum deposit, Jilin Province, NE China, and its Hf isotope significance. *J. Asian Earth Sci.* **2013**, *75*, 58–70. [CrossRef]

24. Zhou, L.-L.; Zeng, Q.-D.; Liu, J.-M.; Friis, H.; Zhang, Z.-L.; Duan, X.-X.; Lan, T.-G. Geochronology of magmatism and mineralization of the Daheishan giant porphyry molybdenum deposit, Jilin Province, Northeast China: Constraints on ore genesis and implications for geodynamic setting. *Int. Geol. Rev.* **2014**, *56*, 929–953. [CrossRef]

25. Ju, N.; Ren, Y.-S.; Wang, C.; Wang, H.; Zhao, H.-L.; Qu, W.-J. Ore genesis and molybdenite Re-Os dating of Dashihe molybdenum deposit in Dunhua, Jilin. *Glob. Geol.* **2012**, *31*, 68–76.

26. Li, L.-X.; Song, Q.-H.; Wang, D.-H.; Wang, C.-H.; Qu, W.-J.; Wang, Z.-G.; Bi, S.-Y.; Yu, C. Re-Os isotopic dating of molybdenite from the Fuanpu Molybdenum deposit of Jilin Province and discussion on Its metallogenesis. *Rock Miner. Anal.* **2009**, *28*, 283–287.

27. Lu, Z.-Q.; Li, X.-J.; Qiu, C.; Liang, B.-S. Geology, geochemistry and geochronology of ore-bearing intrusions in Jidetun molybdenum deposit in mid-east Jilin Province. *Miner. Depos.* **2016**, *35*, 349–364.

28. Zhang, Y. *Research on Characteristics of Geology, Geochemistry and Metallogenic Mechanism of the Jurassic Molybdenum Deposits in the Mid-East Area of Jilin*; Jilin University: Changchun, China, 2013; pp. 1–144.

29. Wang, Q.; Li, Z.-X.; Chung, S.-L.; Wyman, D.A.; Sun, Y.-L.; Zhao, Z.-H.; Zhu, Y.-T.; Qiu, H.-N. Late Triassic high-Mg andesite/dacite suites from northern Hohxil, North Tibet: Geochronology, geochemical characteristics, petrogenetic processes and tectonic implications. *Lithos* **2011**, *126*, 54–67. [CrossRef]

30. Tan, H.-Y.; Lü, J.-C.; Zhang, S.; Kou, L.-L. LA—ICP—MS zircon U-Pb andmolybdenite Re-Os dating for the luming large-scale molybdenum deposit inXiao Hinggan mountains and its geological implication. *Jilin Univ.* **2012**, *42*, 1757–1770.

31. Chen, J.; Sun, F.-Y.; Pan, T.; Wang, J.; Huo, L. Geological features of Huojihe Molybdenum deposit in Heilongjiang, and geochronology and geochemistry of mineralized granodiorite. *Jilin Univ.* **2012**, *42*, 207–215.

32. Yang, Y.-C.; Han, S.-J.; Sun, D.-Y.; Guo, J.; Zhang, S.-J. Geological and geochemical features and geochronology of porphyry molybdenum deposits in the Lesser Xing'an Range–Zhangguangcai Range metallogenic belt. *Acta Pet. Sin.* **2012**, *28*, 379–390.

33. Shu, Q.; Chang, Z.; Lai, Y.; Hu, X.; Wu, H.; Zhang, Y.; Wang, P.; Zhai, D.; Zhang, C. Zircon trace elements and magma fertility: Insights from porphyry (-skarn) Mo deposits in NE China. *Miner. Depos.* **2019**, *54*, 645–656. [CrossRef]

34. Misra, K.C. *Understanding Mineral Deposits*; Kluwer Academic Publishers: Alphen aan den Rijn, The Netherlands, 2000; pp. 353–413.

35. Singer, D.A.; Berger, V.I.; Menzie, W.D. Porphyry copper deposit density. *Econ. Geol.* **2005**, *100*, 491–514. [CrossRef]

36. Ju, N.; Zhang, S.; Zhang, D.; Kou, L.-L. A study on metallogenic epoch and geological characteristic of Chang'anbu Cu-Mo deposit, Shulan City of Jilin Province. *Acta Geol. Sin.* **2015**, *89*, 148–149.

37. Ju, N.; Ren, Y.; Zhang, S.; Kou, L.; Zhang, D.; Gu, Y.; Yang, Q.; Wang, H.; Shi, L.; Sun, Q. The Early Jurassic Chang'anbu porphyry Cu–Mo deposit in Northeastern China: Constraints from zircon U-Pb geochronology and H-O-S-Pb stable isotopes. *Geol. J.* **2017**, *53*, 2437–2448. [CrossRef]

38. Ju, N.; Zhang, S.; Kou, L.-L.; Wang, H.-P.; Zhang, D.; Gu, Y.-C.; Wu, T. Source and Tectonic Setting of Porphyry Mo Deposits in Shulan, Jilin Province, China. *Minerals* **2019**, *9*, 657. [CrossRef]

39. Zhang, D.; Ju, N.; Zhang, S.; Kou, L.-L.; Gu, Y.-C. Geochemical characteristics and geological implication of the ore-forming rocks of the Changanpu Mo(Cu) deposit in Jilin Province. *Geol. Resour.* **2016**, *26*, 253–259.

40. Zhou, Y.; Song, Q.; Zhang, Y.; Wang, Y.; Yu, C. Zircon U-Pb ages and Hf isotope composition of the ore-bearing intrusion from the Chang'anpu Mo-Cu Deposit, Jilin Province. *Gold* **2016**, *37*, 25–29.

41. Han, S.-J.; Sun, J.-G.; Bai, L.-A.; Xing, S.-W.; Chai, P.; Zhang, Y.; Yang, F.; Men, L.-J.; Li, Y.-X. Geology and ages of porphyry and medium-to high-sulphidation epithermal gold deposits of the continental margin of Northeast China. *Int. Geol. Rev.* **2013**, *55*, 287–310. [CrossRef]

42. Wu, F.-Y.; Jahn, B.-M.; Wilde, S.; Sun, D.-Y. Phanerozoic crustal growth: U-Pb and Sr-Nd isotopic evidence from the granites in northeastern China. *Tectonophysics* **2000**, *328*, 89–113. [CrossRef]

43. Jahn, B.-M.; Wu, F.; Chen, B. Massive granitoid generation in Central Asia: Nd isotope evidence and implication for continental growth in the Phanerozoic. *Episodes* **2000**, *23*, 82–92. [CrossRef]

44. Jahn, B.-M.; Capdevila, R.; Liu, D.; Vernon, A.; Badarch, G. Sources of Phanerozoic granitoids in the transect Bayanhongor-Ulaan Baatar, Mongolia: Geochemical and Nd isotopic evidence, and implications for Phanerozoic crustal growth. *Asian Earth Sci.* **2004**, *23*, 629–653. [CrossRef]

45. Pei, Q.-M.; Zhang, S.-T.; Hayashi, K.-I.; Cao, H.-W.; Li, D.; Tang, L.; Hu, X.-K.; Li, H.-X.; Fang, D.-R. Permo-Triassic granitoids of the Xing'an-Mongolia segment of the Central Asian Orogenic Belt, Northeast China: Age, composition, and tectonic implications. *Int. Geol. Rev.* **2018**, *60*, 1172–1194. [CrossRef]

46. Wu, F.-Y.; Sun, D.-Y.; Li, H.; Jahn, B.-M.; Wilde, S. A-type granites in northeastern China: Age and geochemical constraints on their petrogenesis. *Chem. Geol.* **2002**, *187*, 143–173. [CrossRef]

47. Wu, F.-Y.; Sun, D.-Y.; Ge, W.-C.; Zhang, Y.-B.; Grant, M.L.; Wilde, S.A.; Jahn, B.-M. Geochronology of the Phanerozoic granites in northeastern China. *J. Asian Earth Sci.* **2011**, *41*, 1–30. [CrossRef]

48. Jahn, B.-M.; Griffin, W.L.; Windley, B. Continental growth in the Phanerozoic: Evidence from Central Asia. *Tectonophysics* **2000**, *328*, 7–10. [CrossRef]

49. Jahn, B.-M.; Wu, F.; Capdevila, R.; Fourcade, S.; Wang, Y.; Zhao, Z.; Wang, Y. Highly evolved juvenile granites with tetrad REE patterns: The Woduhe and Baerzhe granites from the Great Xing'an (Khingan) Mountains in NE China. *Lithos* **2001**, *59*, 171–198. [CrossRef]

50. Shen, P.; Pan, H.; Hattori, K.; Cooke, D.R.; Seitmuratova, E. Large Paleozoic and Mesozoic porphyry deposits in the Central Asian Orogenic Belt: Geodynamic settings, magmatic sources, and genetic models. *Gondwana Res.* **2018**, *58*, 161–194. [CrossRef]

51. Cao, M.-J.; Li, G.-M.; Qin, K.-Z.; Evans, N.J.; Seitmuratova, E.Y. Assessing the magmatic affinity and petrogenesis of granitoids at the giant Aktogai porphyry Cu deposit, Central Kazakhstan. *Am. J. Sci.* **2016**, *316*, 614–688. [CrossRef]

52. Zhang, L.; Xiao, W.; Qin, K.; Zhang, Q. The adakite connection of the Tuwu-Yandong copper porphyry belt, eastern Tianshan, NW China: Trace element and Sr-Nd-Pb isotope geochemistry. *Miner. Depos.* **2006**, *41*, 188–200. [CrossRef]

53. Goldfarb, R.J.; Taylor, R.D.; Collins, G.S.; Goryachev, N.A.; Orlandini, O.F. Phanerozoic continental growth and gold metallogeny of Asia. *Gondwana Res.* **2014**, *25*, 48–102. [CrossRef]

54. Seltmann, R.; Porter, T.M.; Pirajno, F. Geodynamics and metallogeny of the central Eurasian porphyry and related epithermal mineral systems: A review. *J. Asian Earth Sci.* **2014**, *79*, 810–841. [CrossRef]

55. Natal'in, B.A.; Borukaev, C.B. Mesozoic sutures in the southern Far East of USSR. *Geotectonics* **1991**, *25*, 64–74.

56. Badarch, G.; Cunningham, W.D.; Windley, B.F. A new terrane subdivision for Mongolia: Implications for the Phanerozoic crustal growth of Central Asia. *Asian Earth Sci.* **2002**, *21*, 87–110. [CrossRef]

57. Sengör, A.M.C.; Natal'in, B.A. Paleotectonics of Asia: Fragments of a synthesis. In *The Tectonic Evolution of Asia*; Yin, A., Harrison, M., Eds.; Cambridge University Press: Cambridge, UK, 1996; pp. 486–640.

58. Xiao, W.; Windley, B.F.; Hao, J.; Zhai, M. Accretion leading to collision and the Permian Solonker Suture, Inner Mongolia, China: Termination of the central Asian orogenic belt. *Tectonics* **2003**, *22*, 1069–1090. [CrossRef]

59. Wu, G.; Chen, Y.; Chen, Y.; Zeng, Q. Zircon U-Pb ages of the metamorphic supracrustal rocks of the Xinghuadukou Group and granitic complexes in the Argun massif of the northern Great Hinggan Range, NE China, and their tectonic implications. *Asian Earth Sci.* **2012**, *49*, 214–233. [CrossRef]

60. Chen, Y.-J.; Zhang, C.; Wang, P.; Pirajno, F.; Li, N. The Mo deposits of Northeast China: A powerful indicator of tectonic settings and associated evolutionary trends. *Ore Geol. Rev.* **2017**, *81*, 602–640. [CrossRef]

61. Ge, W.-C.; Lin, Q.; Sun, D.-Y.; Wu, F.-Y.; Won, C.K.; Won, L.M.; Jim, Y.S.; Yun, S.-H. Geochemical characteristics of the Mesozoic basalts in Da Hinggan Ling: Evidence of the mantle-crust interaction. *Acta Pet. Sin.* **1999**, *15*, 397–407.

62. Berdnikov, N.V.; Nevstruev, V.G.; Saksin, B.G. Genetic aspects of the noble metal mineralization at the Poperechnoe deposit, lesser Khingan, Russia. *Pacific Geol.* **2017**, *11*, 421–435. [CrossRef]

63. Didenko, A.N.; Kaplin, V.B.; Malyshev, Y.F.; Shevchenko, B.F. Lithospheric structure and Mesozoic geodynamics of the eastern Central Asian orogen. *Geol. Geophys.* **2010**, *51*, 492–506. [CrossRef]

64. Khanchuk, A.I.; Didenko, A.N.; Popeko, L.I.; Sorokin, A.A.; Shevchenko, B.F. Structure and evolution of the Mongol-Okhotsk orogenic belt. In *The Central Asian Orogenic Belt: Geology, Evolution, Tectonics, and Models*; Kröner, A., Ed.; Borntraeger Science Publishers: Stüttgart, Germany, 2015; pp. 211–234.

65. Berdnikov, N.V.; Nevstruev, V.G.; Kepezhinskas, P.K.; Mochalov, A.G.; Yakubovich, O.V. PGE mineralization in andesite explosive breccias associated with the Poperechnoye iron-manganese deposit (Lesser Khingan, Far East Russia): Whole-rock geochemical, [190]Pt-[4]He isotopic, and mineralogical evidence. *Ore Geol. Rev.* **2020**, *118*, 3352. [CrossRef]

66. Berdnikov, N.V.; Nevstruev, V.G.; Kepezhinskas, P.K.; Astapov, I.; Konovalova, N. Gold in mineralized volcanic systems in the Lesser Khingan Range (Russian Far East): Textural types, composition and possible origins. *Geosciences* **2021**, *11*, 103. [CrossRef]

67. Slama, J.; Kosler, J.; Condon, D.J.; Crowley, J.L.; Gerdes, A.; Hanchar, J.M.; Horstwood, S.A.; Morris, G.A. Plesovice Zircon: A new natural reference material for U-Pb and Hf isotopic microanalysis. *Chem. Geol.* **2008**, *249*, 1–35. [CrossRef]

68. Liu, Y.-S.; Hu, Z.-C.; Gao, S. In Situ Analysis of Major and Trace Elements of Anhydrous Minerals by LA-ICP-MS without Applying an Internal Standard. *Chem. Geol.* **2008**, *257*, 34–43. [CrossRef]

69. Liu, Y.; Hu, Z.; Zong, K.; Gao, C.; Gao, S.; Xu, J.; Chen, H. Reappraisement and refinement of zircon U–Pb isotope and trace element analyses by LA-ICP-MS. *Chin. Sci. Bull.* **2010**, *55*, 1535–1546. [CrossRef]

70. Anderson, T. Correction of common lead in U-Pb analyses that do not report [204]Pb. *Chem. Geol.* **2002**, *192*, 59–79. [CrossRef]

71. Ludwig, K.R. *User's Manual for Isoplot 3.0: A Geochronological Toolkit for Microsoft Excel*; Berkeley Geochron Center Special Publication: Berkeley, CA, USA, 2003; pp. 1–71.

72. Wu, F.-Y.; Yang, Y.-H.; Xie, L.-W.; Yang, J.-H.; Xu, P. Hf isotopic compositions of the standard zircons and baddeleyites used in U-Pb geochronology. *Chem. Geol.* **2006**, *234*, 105–126. [CrossRef]

73. Blichert-Toft, J.; Albarede, F. The Lu-Hf isotope geochemistry of chondrites and the evolution of the mantle-crust system. *Earth Planet. Sci. Lett.* **1997**, *148*, 243–258. [CrossRef]

74. Griffin, W.L.; Wang, X.; Jackson, S.E.; Pearson, N.J.; O'Reilly, S.Y.; Xu, X.-S.; Zhou, X.-M. Zircon chemistry and magma mixing, SE China: In situ analysis of Hf isotopes, Tonglu and Pingtan igneous complexes. *Lithos* **2002**, *61*, 237–269. [CrossRef]

75. Sun, S.-S.; McDonough, W.F. Chemical and isotopic systematics of oceanic basalts: Implications for mantle composition and processes. *Geol. Soc. Lond. Spec. Publ.* **1989**, *42*, 313–345. [CrossRef]

76. Song, Q.-H.; Xing, S.-W.; Zhang, Y.; Li, C.; Wang, Y.; Yu, C. Origin and Geochronology of Chang'anpu Mo-Cu Deposit in Jilin Province: Constraints from Molybdenite Re-Os Isotope Systematics. *Rock Mineral. Anal.* **2016**, *35*, 550–557.

77. Söderlund, U.; Patchett, P.J.; Vervoort, J.D.; Isachsen, C.E. The [176]Lu decay constant determined by Lu-Hf and U-Pb isotope systematics of Precambrian mafic intrusions. Earth Planet. *Sci. Lett.* **2004**, *219*, 311–324.

78. Pearce, J.A.; Harris, N.B.W.; Tindle, A.G. Trace element discrimination diagrams for the tectonic interpretation of granitic rocks. *J. Pet.* **1984**, *25*, 956–983. [CrossRef]

79. Barbarin, B. A review of the relationships between granitoid types, their origins and their geodynamic environments. *Lithos* **1999**, *46*, 605–626. [CrossRef]

80. Sylvester, P.J. Post-collisional alkaline granites. *J. Geol.* **1989**, *97*, 261–280. [CrossRef]

81. Whalen, J.B.; Currie, K.L.; Chappell, B.W. A-type granites: Geochemical characteristics, discrimination and petrogenesis. *Contrib. Mineral. Pet.* **1987**, *95*, 407–419. [CrossRef]

82. Chappell, B.W.; White, A.J.R. Two contrasting granite type. *Pac. Geol.* **1974**, *8*, 173–174.

83. Pitcher, W.S. *Granite Type and Tectonic Environment*; Mountain Building Processes; Academic Press: London, UK, 1982; pp. 19–40.

84. Pitcher, W.S. *The Nature and Origin of Granite Blackie*; Academic and Professional: London, UK, 1993; p. 311.

85. Wu, F.-Y.; Jahn, B.-M.; Wilde, S.A.; Lo, C.-H.; Yui, T.-F.; Lin, Q.; Ge, W.-C.; Sun, D.-Y. Highly fractionated I-type granites in NE China (II): Isotopic geochemistry and implications for crustal growth in the Phanerozoic. *Lithos* **2003**, *67*, 191–204. [CrossRef]

86. Wu, F.-Y.; Li, X.-H.; Zheng, Y.-F.; Gao, S. Lu-Hf isotopic systematics and their application in petrology. *Acta Pet. Sin.* **2007**, *23*, 185–220.

87. Cheng, Y.-B.; Mao, J.-W. Age and geochemistry of granites in Gejiu area, Yunnan province, SW China: Constraints on their petrogenesis and tectonic setting. *Lithos* **2010**, *120*, 258–276.

88. Castillo, P.R.; Janney, P.E.; Solidum, R.U. Petrology and geochemistry of Camiguin island, southern Philippines: Insights to the source of adakites and other lavas in a complex arc setting. *Contrib. Mineral. Pet.* **1999**, *134*, 33–51. [CrossRef]

89. Schiano, P.; Monzier, M.; Eissen, J.P.; Martin, H.; Koga, K.T. Simple mixing as the major control of the evolution of volcanic suites in the Ecuadorian Andes. *Contrib. Mineral. Petr.* **2010**, *160*, 297–312. [CrossRef]

90. Chappell, B.W.; Bryant, C.J.; Wyborn, D. Peraluminous I-type granites. *Lithos* **2012**, *153*, 142–153. [CrossRef]

91. Castillo, P.R. Adakite petrogenesis. *Lithos* **2012**, *135*, 304–316. [CrossRef]

92. Defant, M.J.; Xu, J.-F.; Kepezhinskas, P.; Wang, Q.; Zhang, Q.; Xiao, L. Adakites: Some variations on a theme. *Acta Pet. Sin.* **2002**, *18*, 128–142.

93. Drummond, M.S.; Defant, M.J.; Kepezhinskas, P.K. Petrogenesis of slab-derived trondhjemite- tonalite- dacite/adakite magmas. *Earth Environ. Sci. Trans. R. Soc. Edinburgh.* **1996**, *87*, 205–215. [CrossRef]

94. Cocherine, A. Systematic use of trace element distribution patterns in log-log diagram for plutonic suites. *Geochim. Et. Cosmochim. Acta* **1986**, *1*, 2517–2522. [CrossRef]

95. Peccerillo, A.; Taylor, A.R. Geochemistry of Eocene calc–alkaline volcanic rocks from the Kastamonu area, Northern Turkey. *Contr. Miner. Petro.* **1976**, *58*, 63–81. [CrossRef]

96. Maniar, P.D.; Piccoli, P.M. Tectonic discrimination of granitoids. *Geol. Soc. Am. Bull.* **1989**, *101*, 635–643. [CrossRef]

97. Vervoort, J.D.; Blichert-Toft, J. Evolution of the depleted mantle: Hf isotope evidence from juvenile rocks through time. *Geochim. Et. Cosmochim. Acta* **1999**, *63*, 533–556. [CrossRef]

98. Kinny, P.D.; Maas, R. Lu-Hf and Sm-Nd isotope systems in zircon. *Rev. Mineral. Geochem.* **2003**, *53*, 327–341. [CrossRef]

99. Zhang, Y.; Wu, F.; Wiled, S.A.; Zhai, M.; Lu, X.; Sun, D. Zircon U-Pb ages and tectonic implications of Early Paleozoic granitoids at Yanbian, Jilin Province, northeast China. *Isl. Arc.* **2004**, *13*, 484–505. [CrossRef]

100. Wilkinson, J.J. Triggers for the formation of porphyry ore deposits in magmatic arcs: Predisposition or perfect storm? *Nat. Geosci. Rev. Artic.* **2013**, *10*, 1038–1940.

101. Solomon, M. Subduction, arc reversal, and the origin of porphyry copper-gold deposits in island arcs. *Geology* **1990**, *18*, 630–633. [CrossRef]

102. Richards, J.P. Tectono-magmatic precursors for porphyry Cu-(Mo-Au) deposit formation. *Econ. Geol.* **2003**, *98*, 1515–1533. [CrossRef]

103. Audétat, A. Source and evolution of molybdenum in the porphyry Mo (-Nb) deposit at Cave Peak, Texas. *J. Pet.* **2010**, *51*, 1739–1760. [CrossRef]

104. Audétat, A.; Dolejš, D.; Lowenstern, J.B. Molybdenite saturation in silicic magmas: Occurrence and petrological implications. *J. Pet.* **2011**, *52*, 891–904. [CrossRef]

105. Li, Z.-Z.; Qin, K.-Z.; Li, G.-M.; Ishihara, S.; Jin, L.-Y.; Song, G.-X.; Meng, Z.-J. Formation of the giant Chalukou porphyry Mo deposit in northern Great Xing'an Range, NE China: Partial melting of the juvenite lower crust in untra-plate extensional environment. *Lithos* **2014**, *202–203*, 138–1156. [CrossRef]

106. Fan, W.-M.; Guo, F.; Wang, Y.-J.; Lin, G. Late Mesozoic calc-alkaline volcanism of post-orogenic extension in the northern Da Hinggan Mountains, northeastern China. *J. Volcanol. Geotherm. Res.* **2003**, *121*, 115–135. [CrossRef]

107. Shao, J.-A.; Zang, S.-X.; Mou, B.-L.; Li, X.-B.; Wang, B. Extensional tectonics and asthenospheric upwelling in the orogenic belt: A case study from Hinggan—Mongolia orogenic belt. *Chin. Sci. Bull.* **1994**, *39*, 533–537.

108. Lin, Q.; Ge, W.-C.; Sun, D.-Y.; Wu, F.-Y. Geomechanical significance of the Mesozoic volcanics in Northeast Asia. *Chin. J. Geophys. Chin. Ed.* **1999**, *42*, 75–84.

109. Mao, J.-W.; Wang, Z.-L. A preliminary study on time limits and geodynamic setting of large-scale metallogeny in East China. *Miner. Depos.* **2000**, *19*, 289–296.

110. Muller, D.; Groves, D.I. Potassic igneous rocks and associated gold-copper mineralization. *Miner. Resour. Rev.* **2019**, *53*, 1235–1236.

111. Pearce, J.A. Sources and settings of granitic rock. *Episodes* **1996**, *19*, 120–125. [CrossRef]

112. Wakita, K.; Metcalfe, I. Ocean plate stratigraphy in East and Southeast Asia. *J. Asian Earth Sci.* **2005**, *24*, 679–702. [CrossRef]

113. Yu, J.-J.; Wang, F.; Xu, W.-L.; Gao, F.-H.; Pei, F.-P. Early Jurassic mafic magmatism in the Lesser Xing'an—Zhangguangcai Range, NE China, and its tectonic implications: Constraints from zircon U-Pb chronology and geochemistry. *Lithos* **2012**, *142*, 256–266. [CrossRef]

114. Xiao, W.; Song, D.; Windley, B.F.; Li, J.; Han, C.; Wan, B.; Zhang, J.; Ao, S.; Zhang, Z. Accretionary processes and metallogenesis of the Central Asian Orogenic Belt: Advances and perspectives. *Sci. China Earth Sci.* **2020**, *63*, 329–361. [CrossRef]

115. Wu, F.-Y.; Lin, J.-Q.; Wilde, S.A.; Zhang, X.-O.; Yang, J.-H. Nature and significance of the Early Cretaceous giant igneous event in eastern China. *Earth Planet. Sci. Lett.* **2005**, *233*, 103–119. [CrossRef]

116. Guo, F.; Li, H.; Fan, W.; Li, J.; Zhao, L.; Huang, M.; Xu, W. Early Jurassic subduction of the Paleo-Pacific Ocean in NE China: Petrologic and geochemical evidence from the Tumen mafic intrusive complex. *Lithos* **2015**, *224*, 46–60. [CrossRef]